Sol-gel auto-combustion synthesized ZnMn2O4 for efficient photocatalytic Congo red degradation: structural, kinetics, computational, and ecotoxicity analyses

N. Ahmia, M. Benamira, L. Messaadia, R. Masmoudi, David Horwat, I. Avramova

Sol-gel Auto-combustion Synthesized $ZnMn_2O_4$ for Efficient Photocatalytic Congo Red Degradation: Structural, Kinetics, Computational, and Ecotoxicity Analyses

N. Ahmia[1], M. Benamira[1,*], L. Messaadia[2], R. Masmoudi[3], D. Horwat[4], I. Avramova[5]

[1]*Laboratory of Materials Interaction and Environment (LIME), Faculty of Exact Sciences and Computer Science, University of Jijel, Jijel, Algeria*

[2]*LEAM, Faculty of Exact Sciences and Computer Science, University of Jijel, Jijel, Algeria*

[3]*Laboratory of Chemistry and Environmental Chemistry LCEE, Faculty of Material Sciences, Department of Chemistry, University of Batna 1, Batna, Algeria*

[4] *Université de Lorraine, CNRS, IJL, F-54000 Nancy, France*

[5]*Institute of General and Inorganic Chemistry, Bulgarian Academy of Sciences, Block 11, Acad. G. Bonchev Str, 1113, Sofia, Bulgaria*

*Corresponding author Prof. Benamira Messaoud: m_benamira@univ-jijel.dz

Abstract

$ZnMn_2O_4$ was obtained via the sol-gel auto-combustion method to investigate the photocatalytic degradation of Congo Red (CR) under solar irradiation. Various characterization techniques were employed to determine its structural, morphological, optical, and electrochemical properties. XRD confirmed the tetragonal phase ($I4_1/amd$) with a crystallite size of 20.17 nm. The material exhibited a specific surface area of 37.32 m^2/g. A direct bandgap energy of 1.97 eV was determined. Electrochemical analysis revealed a flat band potential of -0.121 V/SCE, indicating *p*-type behavior. Adsorption kinetics followed a pseudo-second order model, with the Langmuir isotherm providing the best fit, and a monolayer adsorption capacity of 12.155 mg/g. Photocatalytic experiments demonstrated 87.50% CR removal within 3 h under sunlight at a catalyst dosage of 0.8 g/L. The degradation followed pseudo-first order kinetics, with an apparent rate constant (K_{app}) of 0.01074 min^{-1} and a half-life ($t_{1/2}$) of 64.53 min. Photocatalytic efficiency was influenced by photocatalyst dosage, dye concentration, pH, and scavengers. Incorporating TiO_2 improved degradation performance, achieving complete CR removal within 3 h. Recyclability tests confirmed structural stability, with no significant peak

shifts or phase transformations after multiple cycles. DFT calculations classified CR as a soft molecule based on its electronic properties. Monte Carlo simulations demonstrated exceptionally strong interactions in the CR/$ZnMn_2O_4$ system, with an adsorption energy of -16147.31 kcal/mol. Molecular dynamics simulations further verified CR's superior adsorption affinity for $ZnMn_2O_4$ compared to RhB. Notably, ecotoxicity evaluations revealed that the photocatalytic degradation byproducts showed substantially lower acute toxicity than the parent CR compound.

Keywords: $ZnMn_2O_4$; Photocatalysis; Solar Irradiation; Monte Carlo simulation; Molecular dynamics simulations.

1. Introduction

Azo dyes form the most extensive and widely used class of colorants, accounting for 60-70% of global organic dye production [1]. Among them, Congo Red (CR) is a synthetic dye distinguished by its pH-responsive color change and benzidine-derived aromatic structure [2]. As an anionic diazo dye, CR comprises two azo (-N=N-) chromophores and sulfonic ($-SO_3H$) auxochromes, enhancing its solubility in water [3]. Due to its strong coloration properties, it is widely applied in industries such as textiles, plastics, leather, printing, and paper [4]. However, CR exhibits carcinogenic and mutagenic properties, posing risks to human health, including skin irritation, liver damage, and central nervous system disorders, while also negatively impacting aquatic ecosystems [5]. Additionally, toxic byproducts contribute to infertility, allergic reactions, and increased chemical oxygen demand in aquatic environments [6]. The stability and resistance to biodegradation of CR make it a persistent environmental pollutant [7], creating significant challenges for conventional water treatment methods. Given these risks, the development of effective degradation and removal strategies remains a critical research priority.

Photocatalytic degradation has emerged as a pivotal green chemistry technology for treating organic dyes in wastewater [8, 9]. This sustainable and environmentally friendly approach provides high efficiency, minimal secondary contamination, and cost-effectiveness [10, 11]. Unlike conventional methods, which often generate harmful polycyclic byproducts, photocatalysis utilizes solar light to degrade dyes into non-toxic compounds such as carbon dioxide and water [12, 13]. This process relies on semiconductors that, upon light absorption, generate highly reactive species capable of breaking down persistent organic pollutants. Recent

research has emphasized the development of metal oxide nanomaterials as efficient photocatalysts under visible light [14-16]. Their high surface area, abundant active sites, chemical stability, non-toxicity, and low cost make them highly effective for dye degradation [17]. Additionally, their nanoscale size enhances adsorption capacity, further improving photocatalytic performance.

Recent investigations have demonstrated promising results for Congo Red degradation using a variety of photocatalytic systems. Notably, Boulahbel et al. [11] developed a $NiFe_2O_4/TiO_2$ heterostructure via solid dispersion, achieving 97% CR removal after 180 min of sunlight exposure at a concentration of 20 mg/L. A comparable efficiency was reported by Boudiaf et al. [18], who employed a physically mixed $CoAl_2O_4$/ZnO heterosystem under solar irradiation for 4 h at neutral pH. Al-Farraj et al. [19] synthesized $MgAl_2O_4$ nanoparticles using the Pechini sol-gel method, reaching 99.27% degradation within 80 min under UV light at pH 3. Similarly, Zia et al. [20] prepared $ZnSe/Co_3O_4$ heterostructure through a solid-state route, which achieved 96% degradation in just 60 min under UV-visible light. In another approach, Brishti et al. [21] utilized green-synthesized ZnO nanoparticles, which showed 57.6% efficiency at natural pH, increasing to 80.82% under acidic conditions (pH 2). Akhter et al. [22] introduced Ce-doped $Ni_{0.6}Cu_{0.4}Fe_2O_4$ nanostructures via co-precipitation, obtaining 91% degradation under visible light within 100 min. Additionally, Hemamalini et al. [23] demonstrated that $ZnCo_2O_4$ nanoparticles synthesized by co-precipitation removed 61% of CR under sunlight in 2 h. These findings underscore the versatility of metal oxide-based nanomaterials and their potential for effective CR degradation under diverse environmental and operational conditions.

$ZnMn_2O_4$, a spinel-type mixed metal oxide, has attracted significant interest as a photocatalyst due to its distinctive structural, electronic, and redox properties [24, 25]. Its narrow bandgap enables efficient visible-light absorption, while Mn in multiple oxidation states promotes charge separation and electron transfer, thereby suppressing electron-hole recombination. The synergistic interaction between Zn and Mn further enhances photocatalytic activity, improving its efficiency in pollutant degradation. Its chemical stability, non-toxicity, cost-effectiveness, and environmental compatibility underscore its suitability for practical applications [26-28]. Despite these advantages, studies on $ZnMn_2O_4$ for Congo Red degradation remain scarce, warranting further investigation to optimize its photocatalytic performance under visible light.

The photocatalytic performance of a material is profoundly influenced by its synthesis method, as this determines critical properties such as crystallinity, surface area, porosity, optical behavior, and electronic structure [6, 29-30]. Among various synthesis techniques, the sol-gel

auto-combustion method stands out for its ability to produce nanomaterials with high purity, uniform particle size distribution, and enhanced crystallinity [31, 32]. This approach facilitates the formation of a well-defined spinel structure, which contributes to charge separation and helps suppress electron-hole recombination. Furthermore, the exothermic nature of the auto-combustion process generates porous architectures [33, 34], significantly increasing the catalyst's surface area and adsorption capacity, thereby enhancing its photocatalytic activity [35].

Computational simulations provide critical atomic-level insights into adsorption mechanisms, complementing experimental studies by revealing interaction energies, molecular orientations, and dynamic behavior of adsorbates on photocatalyst surfaces [36]. Among these techniques, the Monte Carlo (MC) method facilitates statistical sampling of possible configurations to identify energetically favorable adsorption sites, guided by Boltzmann-distributed probabilities [37]. This approach is particularly effective in capturing equilibrium behavior at interfaces and mapping out potential energy landscapes of dye-surface systems [36]. Simultaneously, Molecular Dynamics (MD) simulations model the temporal evolution of adsorbate-surface interactions, capturing dynamic processes such as solvation, diffusion, and conformational adjustments at finite temperatures [38–40]. MD simulations also enable the observation of desorption events, hydrogen bonding evolution, and rearrangement of surface hydration layers, which are critical in photocatalytic environments [41]. These techniques collectively provide a comprehensive framework for understanding interfacial behavior under realistic conditions, guiding the rational design of materials for environmental remediation.

This study aims to investigate the photocatalytic degradation of Congo Red (CR) using $ZnMn_2O_4$ under solar light irradiation, with a focus on efficiency across various operational conditions. The degradation pathway is analyzed through radical scavenging experiments. To complement the experimental findings, Density Functional Theory (DFT) calculations are employed to model the CR molecule in aqueous media and assessing both global and local reactivity. The most susceptible regions of the molecule are identified using Fukui functions, the dual descriptor (f_k^2), and local parameters such as softness ($\Delta\sigma_k$) and philicity ($\Delta\omega_k$). Additionally, Monte Carlo and Molecular Dynamics simulations are conducted to compare the adsorption behavior of CR and Rhodamine B (RhB) on the $ZnMn_2O_4$ surface. The environmental and toxicological impacts of CR and its degradation intermediates are further assessed through theoretical predictions of Daphnia magna LC_{50} (48 h), Oral rat LD_{50}, and Bioconcentration factor (BCF) values.

2. Materials and methods

2.1. Synthesis

Zinc manganese oxide ($ZnMn_2O_4$) was prepared using the sol-gel auto-combustion process, as shown in **Fig. S1**. Zinc nitrate hexahydrate ($Zn(NO_3)_2 \cdot 6H_2O$, >96%, Sigma-Aldrich), manganese nitrate monohydrate ($Mn(NO_3)_2 \cdot H_2O$, >98%, Sigma-Aldrich), and citric acid ($C_6H_8O_7$, >99%, Sigma-Aldrich) were used as starting precursors. A Zn:Mn molar ratio of 1:2 was maintained by dissolving 2.90 g of $Zn(NO_3)_2 \cdot 6H_2O$ (0.01 mol) and 4.96 g of $Mn(NO_3)_2 \cdot H_2O$ (0.02 mol) in 40 mL of distilled water. Subsequently, an aqueous solution of citric acid (2.42 g in 40 mL) was added to the metal nitrate mixture under continuous magnetic stirring. The solution was then heated at 90 °C for 120 min to form a homogeneous gel. The temperature was further increased to 300 °C, triggering spontaneous auto-combustion due to evaporation. The resulting powder was ground and calcined at 400 °C for 4 h with a heating rate of 5 °C/min to obtain the $ZnMn_2O_4$ powder. The global reaction can be expressed as follows:

$$Zn(NO_3)_2 + 2\ Mn(NO_3)_2 + x\ C_6H_8O_7 \rightarrow ZnMn_2O_4 + y\ CO_2 + z\ H_2O + \gamma\ N_2 \qquad (1)$$

Anatase-phase TiO_2, used for the preparation of the $ZnMn_2O_4/TiO_2$ heterojunction, was synthesized via a sol–gel method. Tetrabutyl titanate ($Ti(OC_4H_9)_4$, ≥97%, Sigma-Aldrich) was dissolved in a methanol/ethanol mixture with a molar ratio of 1:1:10 under continuous stirring. The solution was heated at 75 °C for 3 h to promote hydrolysis and condensation. Deionized water was then added dropwise to initiate gel formation. The resulting gel was dried at room temperature overnight and subsequently calcined at 450 °C for 2 h to obtain crystalline anatase TiO_2. The $ZnMn_2O_4/TiO_2$ heterojunction was prepared by physically mixing the as-synthesized TiO_2 powder with $ZnMn_2O_4$. The powders were blended in specific weight ratios to ensure homogeneous dispersion and to achieve the desired composition.

2.2. Characterizations

X-ray diffraction (XRD) was utilized to investigate the crystalline structure, using Cu-Kα monochromatic radiation (λ = 1.54056 Å) across a 2θ range of 15° to 80°. The obtained diffraction data were analyzed with the HighScore Plus software. The Fourier Transform Infrared (FT-IR) spectrum was recorded over a wavenumber range of 500 to 4000 cm^{-1} using a Bruker spectrometer. The specific surface area was determined using the Brunauer-Emmett-

Teller (BET) method with a Micromeritics Tristar 3000 analyzer. The sample was degassed under vacuum for 2 h before cooling and undergoing adsorption-desorption analysis.

The morphology and composition of the as-prepared powder were analyzed using a Zeiss EVO 15 scanning electron microscope (SEM) equipped with Energy-Dispersive X-Ray Spectroscopy (EDS). Transmission electron microscopy (TEM) was performed with a Thermo Fisher Talos F200X electron microscope operating at voltages ranging from 80 to 220 kV. The diffuse reflectance spectrum was obtained over the wavelength range of 350-1000 nm using a Specord 200 Plus UV-Vis. spectrophotometer. X-ray photoelectron spectroscopy (XPS) analysis was performed using a VG ESCALAB MKII electron spectrometer operated under a base pressure of 10^{-8} Pa, employing Al Kα radiation (1486.6 eV) as the excitation source. The C 1s peak at 285.0 eV was used as the reference for binding energy (BE) calibration, with a measurement accuracy of 0.2 eV. Spectral fitting and deconvolution were conducted using CasaXPS software.

The surface charge properties of the synthesized $ZnMn_2O_4$ powder were evaluated by determining the point of zero charge (pH_{pzc}) through the pH drift method. A series of 50 ml NaCl solutions (0.01 M) were prepared, each containing 0.1 g of the sample. The pH of the solutions was adjusted with HCl and NaOH, and the mixtures were allowed to equilibrate for 24 hours at room temperature in an isothermal shaker. The pH_{pzc} value was identified as the point where the initial and final pH values intersected.

Electrochemical measurements were performed at room temperature using an OrigaLys potentiostat, with a saturated calomel electrode (SCE) as the reference electrode and a platinum electrode (Pt) as the counter electrode. Mott-Schottky (M-S) plots were obtained in a 0.5 M Na_2SO_4 electrolyte at a frequency of 10 kHz. The corrosion current of $ZnMn_2O_4$ in Na_2SO_4 electrolyte and Congo Red (CR) was determined through current-voltage (J–V) analysis using a semi-logarithmic Tafel plot (log J–E).

2.3. Photocatalysis

To study the photodegradation of Congo Red (CR), 80 mg of $ZnMn_2O_4$ powder was dispersed in 100 mL of an aqueous CR solution (20 mg/L) within a Pyrex cell. The mixture was stirred in the dark at room temperature until adsorption equilibrium was reached. The suspension was then exposed to sunlight (~105 mW/cm^2) for 3 h, with an average ambient temperature of 27 ± 2°C and relative humidity of 60 ± 5%. Aliquots of 5 mL were collected at regular intervals, centrifuged at 2000 rpm for 15 min. All photocatalytic experiments

were conducted outdoors in Jijel, Algeria, on a sunny day in June, between 11:00 a.m. and 3:00 p.m, local time (peak solar irradiance). Absorbance measurements were recorded using an Optizen Pop UV-visible spectrophotometer, and CR degradation was calculated using Eq. (2) [12]:

$$\%\ of\ photodegradation = (\frac{C_0 - C_t}{C_0}) \times 100 \qquad (2)$$

Where C_0 and C_t represent the initial concentration and the concentration of Congo Red (CR) at time (t), respectively.

The amount of CR adsorbed (q_t) was calculated using the following expression (Eq. (3)) [14]:

$$q_t = (\frac{C_0 - C_t}{m}) \times V \qquad (3)$$

Where V represents the solution volume and m denotes the adsorbent mass used.

2.4. Computational Chemistry Study

2.4.1. Density Functional Theory

Density Functional Theory (DFT) calculations were carried out using the Dmol^3 module within BIOVIA Materials Studio software. The geometry optimization of the CR molecule in an aqueous medium was conducted utilizing the Perdew-Burke-Ernzerhof (PBE) functional within the Generalized Gradient Approximation (GGA) to assess molecular reactivity. The Double Numerical Plus Polarization (DNP) 4.4 basis set was employed for atomic orbitals. The convergence criteria included a self-consistent field (SCF) tolerance of 10^{-6} Hartree (Ha), a maximum displacement between cycles of less than 0.005 Å, and a maximum per-atom force of 0.002 Ha/Å. Additionally, a global orbital cutoff of 4.5 Å was applied to refine parameters governing atomic orbital interactions. The solvent environment (water, dielectric constant ε = 78.54) was simulated using the Conductor-like Screening Model (COSMO).

2.4.2. Electrostatic Potential Surface

The Electrostatic Potential Surface (EPS) is a powerful tool for analyzing the reactivity of chemical compounds by mapping the spatial distribution of electrostatic potential across molecular surfaces. This method employs a color-coded system to delineate regions of varying electron density and charge distribution. Areas depicted in blue indicate the highest positive electrostatic potential, by electron deficiency and a corresponding positive charge, rendering them optimal sites for nucleophilic interactions. Conversely, yellow-shaded regions represent the lowest negative electrostatic potential, typically associated with heteroatoms such as

chlorine, nitrogen, or sulfur, which exhibit susceptibility to electrophilic attack. Meanwhile, green areas denote neutral or zero potential regions, where the electrostatic charge is negligible, indicating minimal reactivity.

2.4.3. Fukui Indices and Dual Descriptor

Fukui indices represent a fundamental concept in computational chemistry, particularly within the framework of Density Functional Theory (DFT). These indices serve as predictive tools for molecular reactivity by identifying regions most susceptible to nucleophilic, electrophilic, or radical attacks. The Fukui functions are formally defined as follows [8]:

$$f_k^+ = q_k(N+1) - q_k(N) \approx \rho(r)^{LUMO} \quad \text{(For nucleophilic attack)} \quad (4)$$

$$f_k^- = q_k(N) - q_k(N-1) \approx \rho(r)^{HOMO} \quad \text{(For electrophilic attack)} \quad (5)$$

$$f_k^0 = [q_k(N+1) - q_k(N-1)]/2 \quad \text{(For radical attack)} \quad (6)$$

Here, $q_k(N+1)$, $q_k(N)$ and $q_k(N-1)$ denote the atomic charges of atom (k) in the anionic, neutral, and cationic states, respectively.

The dual descriptor (f_k^2), commonly referred to as the second-order Fukui function, offers a more comprehensive evaluation of electron transfer processes within a molecule. By extending the conventional Fukui function framework, it effectively distinguishes atomic sites according to their propensity for nucleophilic or electrophilic interactions [42, 43]. A positive $f_k^2\ (r)$ value at a given site indicates a greater propensity to accept electrons, signifying enhanced reactivity toward nucleophiles species. Conversely, a negative $f_k^2\ (r)$ value identifies regions more susceptible to electrophilic attack, as these sites exhibit a higher tendency to lose electron density, rendering them favorable for electrophilic interactions. The local philicity ($\Delta\omega_k$) and local softness ($\Delta\sigma_k$) are fundamental descriptors utilized to assess the reactivity of individual atomic sites within a molecule. These parameters are formally defined as: $\omega_k^\propto = \omega f_k^\propto$ and $\sigma_k^\alpha = S f_k^\propto$.

where ω and S denote the global philicity and global softness, respectively, while $f_k^\propto$ represents the Fukui function at atomic site (k), corresponding to a specific type of chemical attack (α).

2.4.4. Monte Carlo and Molecular Dynamics Simulations

Monte Carlo (MC) and Molecular Dynamics (MD) simulations were conducted using Materials Studio to investigate the adsorption behavior of Congo Red (CR) and Rhodamine B (RhB) on

$ZnMn_2O_4$ surfaces in an aqueous phase comprising 200 water molecules. The Adsorption Locator module was employed in the MC approach to determine the most energetically favorable configurations of dye molecules on the surface. Molecular structures were geometry-optimized utilizing the Condensed-phase Optimized Molecular Potentials for Atomistic Simulation Studies II (COMPASSII) force field to ensure computational accuracy.

For the MD simulations, the $ZnMn_2O_4$ (211) surface was constructed based on XRD and DFT results and modeled within a periodic simulation box of dimensions 81.246 Å × 49.123 Å × 39.694 Å. A cleaved thickness of 3 Å, an 8 × 8 supercell, and a 30 Å vacuum layer were implemented to ensure accurate modeling and mitigate boundary effects. Simulations were performed using the Forcite module under the canonical ensemble (NVT: constant number of particles, volume, and temperature) at 298 K, with a time step of 1 fs for a total simulation period of 500 ps. Interaction energies ($E_{Interaction}$) and binding energies ($E_{Binding}$) were computed as follows [24]:

$$E_{\text{Interaction}} = E_{\text{Totale}} - (E_{\text{Surface + 200 H2O}} + E_{\text{Dye}}) \quad (7)$$

$$E_{\text{Binding}} = -E_{\text{Interaction}} \quad (8)$$

Where E_{Total} denotes the total energy of the system ($ZnMn_2O_4$/Dye/H_2O), ($E_{Surface + 200\ H2O}$) represents the total energy of the $ZnMn_2O_4$ semiconductor surface with 200 water molecules, and (E_{Dye}) corresponds to the energy of the dye molecule.

2.4.5. Toxicity Assessment

The Toxicity Estimation Software Tool (TEST) was utilized to evaluate the potential toxicity of the Congo Red (CR) dye and its intermediates. TEST employs Quantitative Structure-Activity Relationship (QSAR) methodologies to estimate toxicity through various predictive modules, including Daphnia magna LC_{50} (48hr; 50% lethal concentration), oral rat LD_{50} (50% lethal dose) and the Bioconcentration factor (BCF). The Consensus method was applied to enhance the accuracy and reliability of toxicity predictions.

3. Results and Discussion

3.1. Structural, Morphological and Optical Properties

Fig. 1a presents the XRD pattern of $ZnMn_2O_4$ following calcination at 400 °C for 4 h. The diffraction peaks align with the tetragonal structure of the $I4_1/amd$ space group, as confirmed

by JCPDS Card No. 01-077-0470. Notable peaks appear at approximately 18.21°, 29.27°, 31.19°, 32.77°, 36.32°, 38.83°, 44.87°, 51.56°, 54.21°, 56.65°, 58.97°, 60.81°, 65.08°, and 74.83°, correspond to the crystallographic planes (101), (112), (200), (103), (211), (004), (220), (105), (312), (303), (321), (224), (400), and (413). Additionally, a secondary phase of hexagonal zinc oxide (ZnO) is identified at a peak of 47.31°, corresponding to the $P6_3mc$ space group (JCPDS Card No. 01-079-0208). The crystallite size (D) of $ZnMn_2O_4$ is determined to be 20.17 nm, calculated based on the broadening of the (211) XRD peaks using the Scherrer equation.

The FTIR analysis of the $ZnMn_2O_4$ nanomaterial was performed within the wavenumber range of 4000 cm^{-1} to 550 cm^{-1} to identify the functional groups present its surface **(Fig. S2a)**. The spectrum exhibits a band at 2344 cm^{-1}, corresponding to the asymmetric stretching of O-C-O in CO_2. A peak at 1629 cm^{-1} attributed to the stretching vibration of the C=C bond. Additionally, a distinct peak at 1076 cm^{-1} is associated with Mn-O-H vibrations. Peaks observed between in the 500 cm^{-1} to 700 cm^{-1} range are linked to Zn-O and Mn-O bonds.

The BET method is utilized to assess the specific surface area (S_{BET}) and porosity of $ZnMn_2O_4$ powder. The S_{BET} values are calculated from the nitrogen adsorption-desorption isotherms depicted in **Fig. S2b**. Based on IUPAC classification, the isotherm for $ZnMn_2O_4$ is identified as a type IV isotherm with H3 type hysteresis loops, indicating the presence of mesopores. The BET surface area is found to be 37.32 m^2/g.

The SEM micrograph (**Fig. 1b**) reveals that the $ZnMn_2O_4$ particles form aggregated clusters composed of nanoscale crystallites. While some regions exhibit a quasi-spherical appearance, the overall morphology is heterogeneous, characterized by irregular shapes and partial agglomeration. The particle size is estimated to range from 50 to 80 nm.

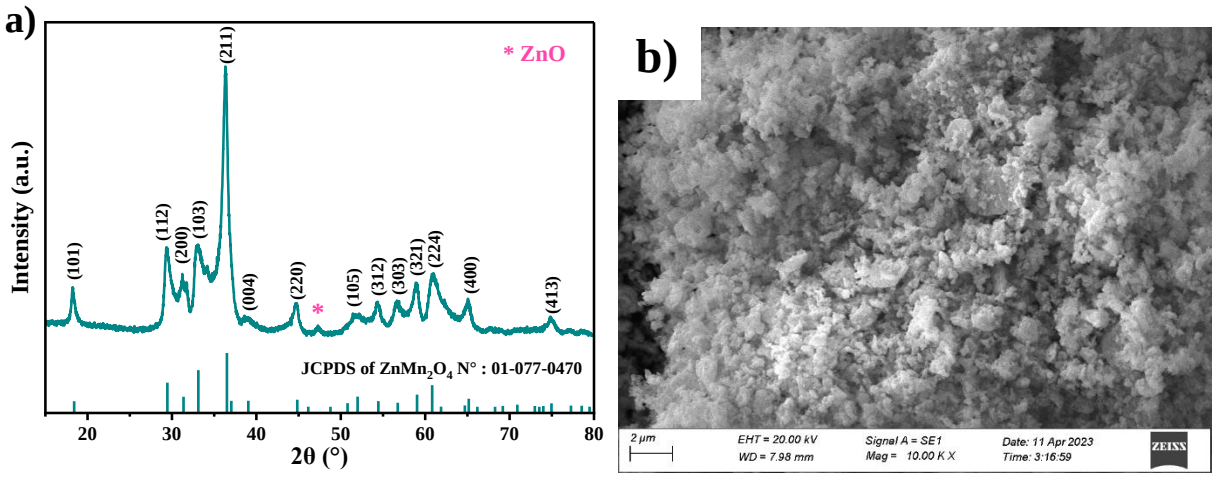

Fig. 1. a) X-ray diffraction, b) SEM image of $ZnMn_2O_4$.

TEM analysis of $ZnMn_2O_4$ was performed to provide detailed insight into its morphology and microstructure. As shown in **Fig. 2a**, the particles display a range of shapes, including sub-spherical and irregular geometries, indicating notable morphological diversity. Despite this variation in form, the particle dimensions are relatively consistent, ranging from 15 to 40 nm, which aligns closely with the crystallite sizes estimated from XRD analysis. The high-resolution TEM (HRTEM) image indicates an interplanar d-spacing of 0.244 nm, which coincides with the (211) crystallographic plane (**Fig. 2b**). This prominent plane suggests a high level of crystallinity in the nanoparticles. The selected area electron diffraction (SAED) pattern (**Fig. 2c**) is accurately indexed to the (112), (200), (103), (211), (220), (312), (303), (321), and (400) planes of $ZnMn_2O_4$, confirming its polycrystalline nature.

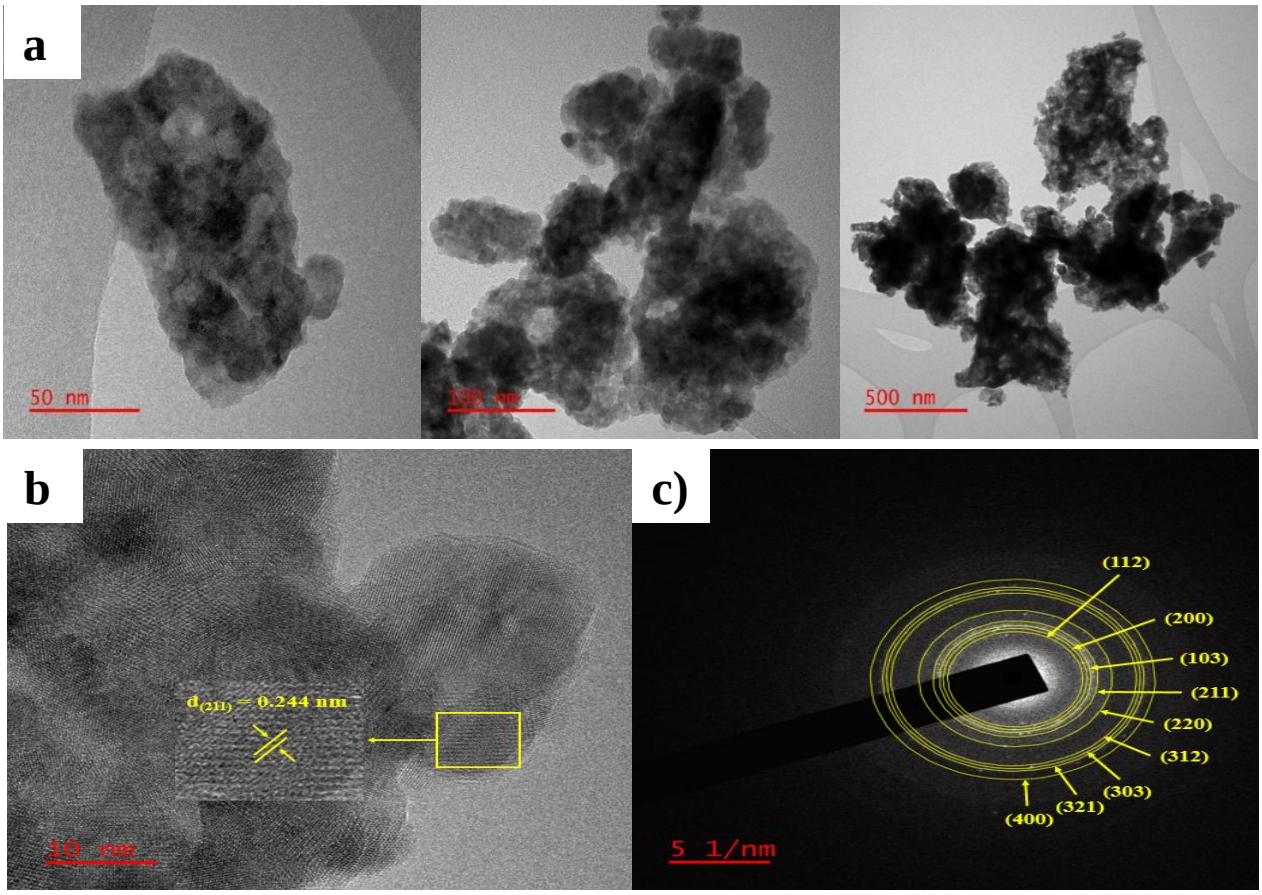

Fig. 2. a) TEM images, b) HRTEM image, c) SAED pattern of $ZnMn_2O_4$.

XPS was utilized to investigate the elemental composition and oxidation states present in $ZnMn_2O_4$, as shown in **Fig. 3.** The survey spectrum confirmed the existence of Zn, Mn, and O within the material (**Fig. 3a**). The O 1s spectrum (**Fig. 3b**) displayed two distinct components, with a primary peak at 529.64 eV, assigned to lattice oxygen (O^{2-}), and a secondary peak at 531.34 eV, attributed to chemisorbed oxygen species (O_{ads}) [44]. The Zn 2p region (**Fig. 3c**) exhibited spin-orbit doublets at 1020.64 eV (Zn $2p_{3/2}$) and 1043.70 eV (Zn $2p_{1/2}$), characteristic of Zn^{2+} ions, with a 23.06 eV energy separation [45, 46]. The Mn 2p spectrum (**Fig. 3d**) revealed peaks at 640.68 eV and 652.27 eV, corresponding to Mn $2p_{3/2}$ and Mn $2p_{1/2}$, respectively. The 11.59 eV spin-orbit separation between the Mn $2p_{3/2}$ and Mn $2p_{1/2}$ peaks is consistent with the presence of Mn^{3+} as the dominant oxidation state, while the slightly lower binding energy of Mn $2p_{3/2}$ suggests the possible coexistence of other oxidation states within the structure [46].

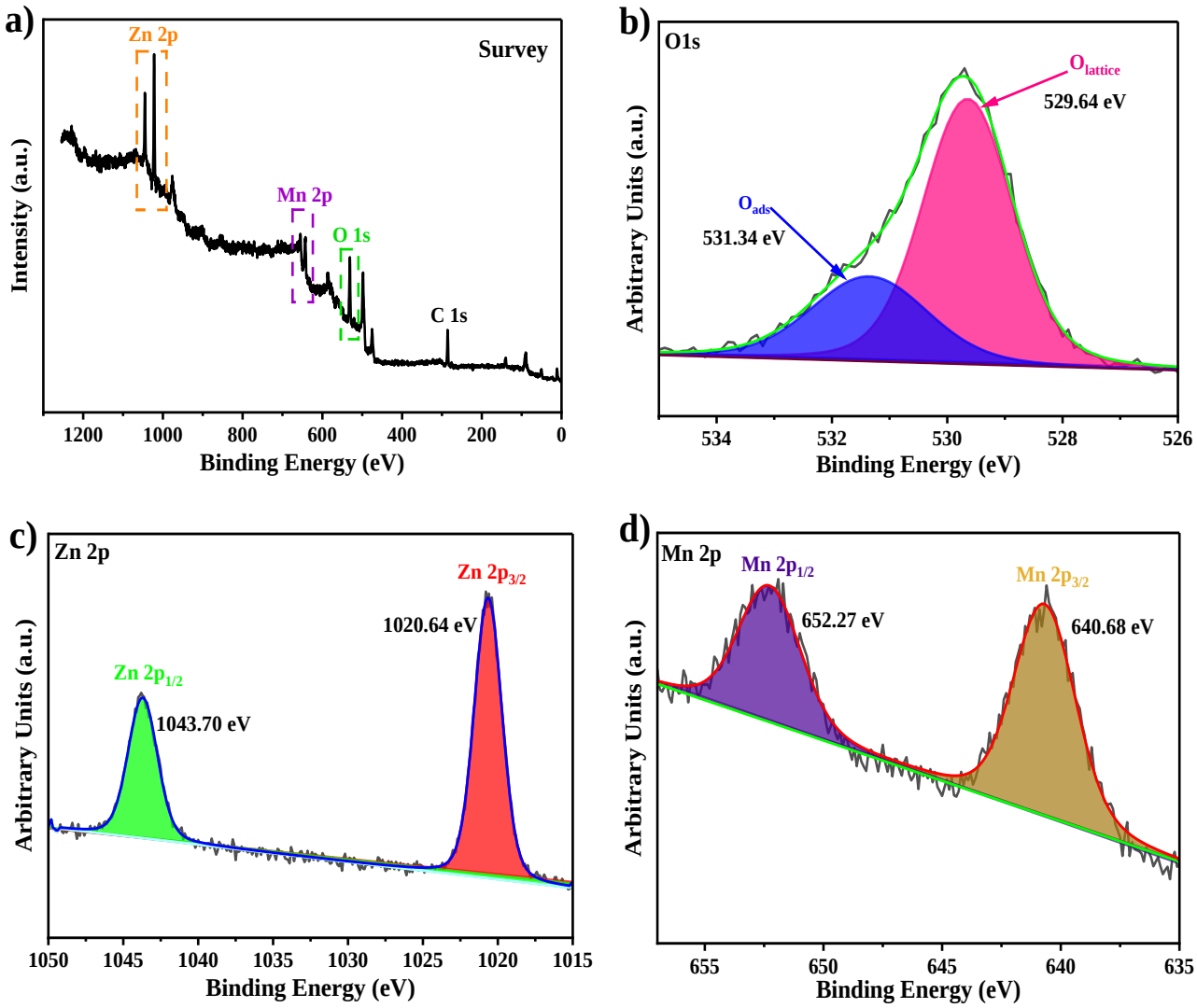

Fig. 3. a) XPS survey spectrum of the spinel $ZnMn_2O_4$. Core-level XPS spectra of the elements present in $ZnMn_2O_4$, b) O1s, c) Zn 2p and d) Mn 2p.

The optical absorption properties of a semiconductor are strongly linked to its band gap and electronic structure, both of which significantly influence electron migration. Consequently, UV-Vis diffuse reflectance spectroscopy (DRS) is a crucial technique for indirectly evaluating the photocatalytic activity of semiconductors. This method was employed to analyze the light absorption behavior and band gap of the $ZnMn_2O_4$ sample (**Fig. 4a**). The following relation was used to calculate the optical band gap (E_g) [11]:

$$E_g(eV) = 1240/\lambda_0\ (nm) \qquad (9)$$

Where E_g is the band gap energy and λ_0 is the wavelength at the absorption edge. This wavelength represents the longest photon wavelength that can promote an electron from the valence band to the conduction band, thereby generating an electron–hole pair.

The value of λ_o was determined from the inflection point of the reflectance spectrum by plotting the first derivative of the diffuse reflectance ($dR/d\lambda$) versus wavelength (**Fig. 4a**). The absorption edge was found at 647 nm, corresponding to a band gap energy of 1.92 eV.

To further analyze the optical properties, the obtained reflectance spectra can be transformed into absorption spectra using the Kubelka−Munk function F(R), as shown in Eq. (10).

$$F(R) = \frac{(1-R)^2}{R} \qquad (10)$$

Where R denotes the diffuse Reflectance

This conversion enables the estimation of the optical band gap energy (Eg) using a modified Tauc equation (Eq. (11))**.**

$$(F(R) * h\nu)^{1/n} = A\,(h\nu - E_g) \qquad (11)$$

Where h denotes Planck's constant, ν represents the frequency of the photon, and A is a constant. The parameter n is associated with the type of electronic transition, taking a value of 1/2 for direct allowed transitions and 2 for indirect allowed transitions.

The band gap of the synthesized $ZnMn_2O_4$ was determined by extrapolating the linear portion of the $(F(R) * h\nu)^{1/n}$ plot with the $h\nu$ photon energy axis. For n=1/2, corresponding to a direct allowed transition, the estimated band gap was 1.97 eV (**Fig. 4b**). In contrast, the plot using n=2, which corresponds to an indirect allowed transition (**Fig. 4c**), yielded a significantly lower band gap value of 1.05 eV. This latter value deviates considerably from the band gap previously estimated (1.92 eV) using the first derivative of the diffuse reflectance spectrum. This discrepancy suggests that the optical transitions in $ZnMn_2O_4$ are more likely direct in nature.

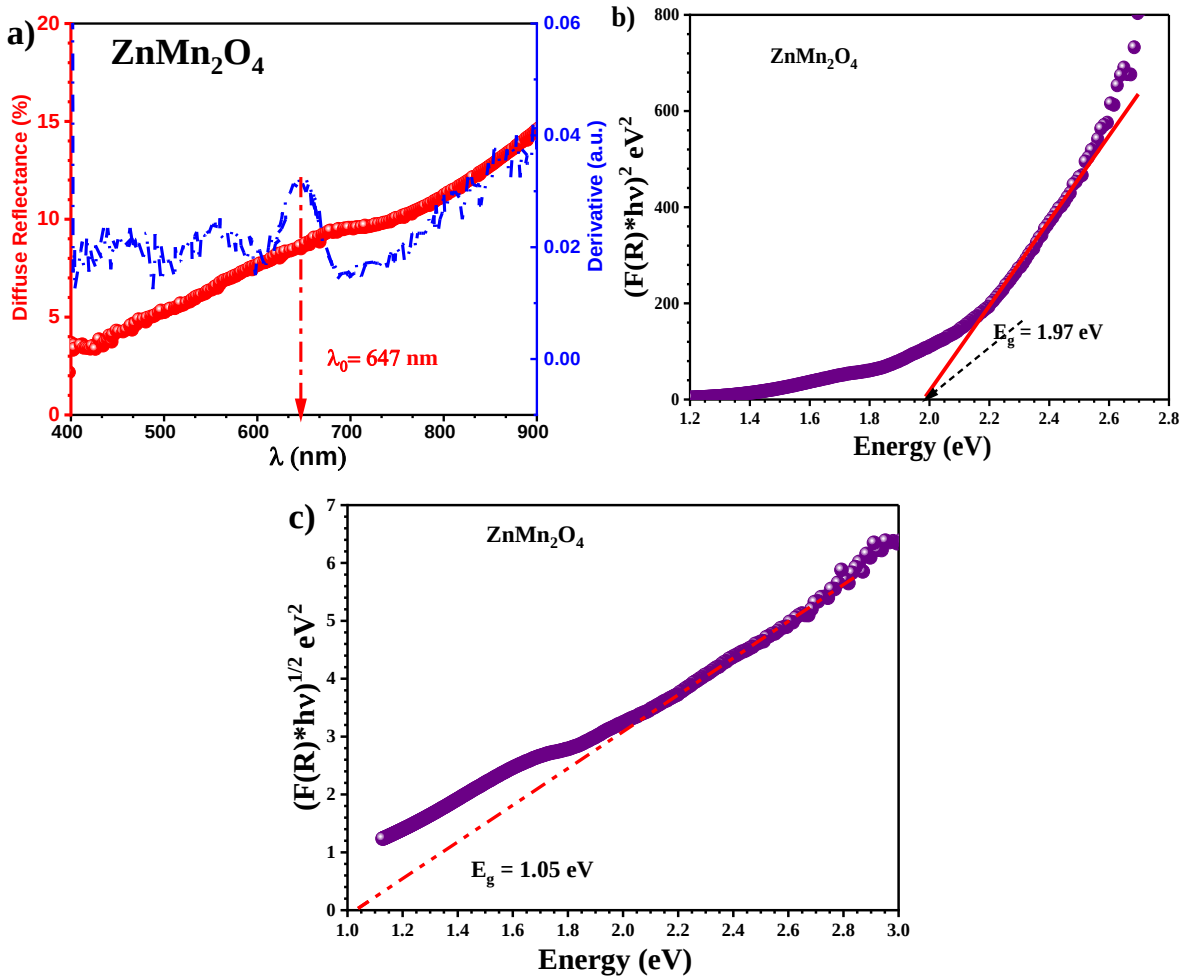

Fig. 4. a) UV-Vis diffuse reflectance spectrum, b) direct optical transition of $ZnMn_2O_4$, c) Indirect optical transition of $ZnMn_2O_4$.

3.2. Electrochemical characterization

Estimating the flat-band potential (E_{fb}) is crucial for understanding the electronic structure of semiconductors, evaluating their photocatalytic performance, and analyzing interfacial charge transfer mechanisms. This parameter is derived from the Mott-Schottky plot, which correlates interface capacitance with applied potential, as described by the following equation [47]:

$$\frac{1}{C_{SC}^2} = \left(\frac{2}{e \times \varepsilon_r \times \varepsilon_0 \times N_d \times A^2}\right) \times \left(\left(E - E_{fb}\right) - \frac{KT}{e}\right) \qquad (12)$$

Where N_d denotes the free carrier density and E represents the applied potential.

The flat-band potential (E_{fb}) of $ZnMn_2O_4$ was determined from the $\frac{1}{C_{SC}^2}$ versus *V* plot (**Fig. 5)**. The negative slope of the linear region confirmed its p-type nature, and extrapolation to the x-axis yielded an E_{fb} of -0.121 V/SCE.

The current-voltage (J–V) curves for $ZnMn_2O_4$, recorded in a 0.5 M Na_2SO_4 electrolyte and a Congo Red (20 ppm) solution, are shown in **Fig. S3**. In Na_2SO_4, the exchange current density is around 1.9 μA/cm^2, which decreases slightly to 1.5 μA/cm^2 in the CR solution, indicating a minor alteration in the electrochemical behavior of $ZnMn_2O_4$. This reduction suggests interactions between CR molecules and the $ZnMn_2O_4$ surface, potentially hindering charge transfer at the electrode interface. Furthermore, the equilibrium potential (i = 0) shifts notably from 250.1 mV in Na_2SO_4 to 310.2 mV in the CR solution. The stable current behavior in both electrolytes highlights the robust electrochemical stability of $ZnMn_2O_4$, supporting its potential for photocatalytic dye degradation applications.

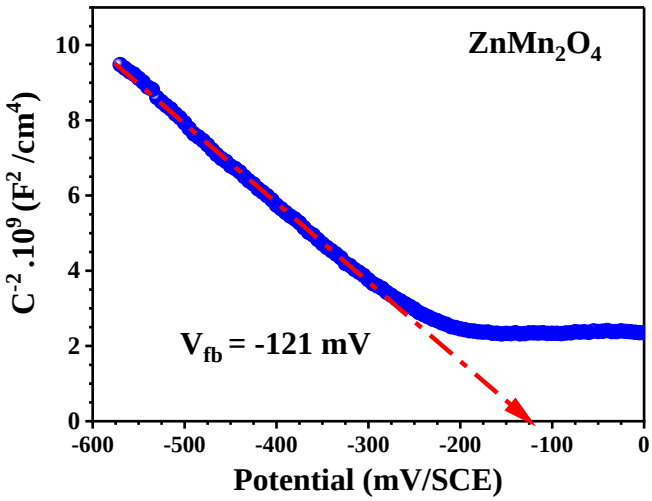

Fig. 5. The (C^{-2} – V) plots for the $ZnMn_2O_4$/Na_2SO_4 (0.5 M, pH ~ 7.3) system.

3.3. Energy band diagram

Based on the experimental findings from optical and electrochemical tests, the energy band diagram of p-$ZnMn_2O_4$ can be constructed, illustrating the relative positions of the valence band (VB) and conduction band (CB). This diagram aids in predicting the material's efficiency in degrading organic pollutants, emphasizing the role of reactive radicals such as hydroxyl ($^{\bullet}OH$) and superoxide ($O_2^{\bullet-}$). The energy positions of the valence and conduction bands can be determined using the following equations [48]:

$$E_{VB} = eV_{fb} + 0.059\,(pH - pH_{PZC}) + E_a \qquad (p-type) \qquad (13)$$

$$E_{VB}(vs.vacuum) = E_f - E_{VB}\,(vs.NHE) \qquad (14)$$

$$E_{CB} = E_{VB} - E_g \qquad (15)$$

Where pH_{pzc} and E_f represent the zero charge point and free electron energy on the hydrogen scale, respectively.

The Point of Zero Charge (PZC) is a fundamental parameter in surface chemistry that defines the pH at which a material's surface carries no net electrical charge. It plays a critical role in adsorption, as it varies with material properties. At the pH_{pzc}, the adsorbent surface exhibits a balance of positive and negative charges. For $ZnMn_2O_4$, the pH_{pzc} was determined to be 7.28 using the pH drift method (**Fig. 6a**). When the solution pH is below this value, the $ZnMn_2O_4$ surface becomes positively charged, enhancing electrostatic attraction with anionic CR molecules and thereby increasing adsorption capacity. Above the pH_{pzc}, the surface carries a negative charge, which hinders anionic dye adsorption.

Fig. 6b presents the energy band diagram configuration of the $ZnMn_2O_4$/CR electrolyte interface at a pH of approximately 6.1. The narrow band gap of 1.97 eV enables the generation of electron-hole (e^-/h^+) pairs. Upon solar irradiation, photogenerated electrons in the valence band (0.16 V_{SCE}) are effectively transferred to the conduction band (-1.81 V_{SCE}) of p-type $ZnMn_2O_4$.

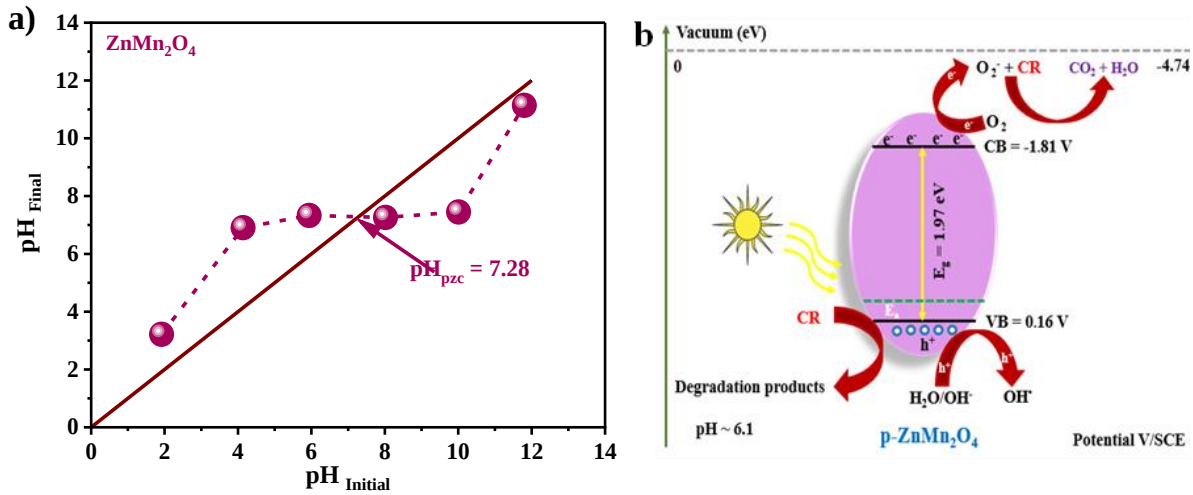

Fig. 6. a) Determination of the pH_{pzc} of $ZnMn_2O_4$, b) Energy band diagram of *p*-$ZnMn_2O_4$/CR electrolyte at pH ~ 6.1.

3.4. Adsorption study

The protonation state plays a crucial role in influencing binding mechanisms and adsorption efficiency across various pH levels, making it essential for optimizing adsorption processes. To examine the protonation behavior of CR over a pH range of 0 to 14, MarvinSketch software was utilized. The species distribution diagram and the predominant forms of CR are depicted in **Fig. 7a**. Across the entire pH range studied, a single predominant form characterized by the (SO_3^-) group is evident, demonstrating the stability of the molecule under acidic, neutral and alkaline conditions.

The pKa values help predict the protonation behavior of molecules, which is crucial for understanding their interactions in catalytic or photocatalytic reactions, particularly in dye degradation processes. **Fig. 7b** illustrates the protonation sites of the Congo Red molecule. The first site, with a pKa of -1.78, corresponds to a sulfonic acid group (-SO_3H), indicating a strong acid that remains deprotonated even under highly acidic conditions. The second and fifth sites, both amine groups (-NH_2), share a pKa of -0.88, suggesting minimal protonation except at extremely low pH. The third site, a nitrogen atom, has a pKa of 0.21, reflecting a comparatively higher tendency to accept a proton. The fourth site, another nitrogen, shows a pKa of -0.42, indicating lower proton affinity. Moreover, the sixth site, also a sulfonic acid group, exhibits the lowest pKa (-2.37), identifying it as the most acidic site and highly prone to deprotonation.

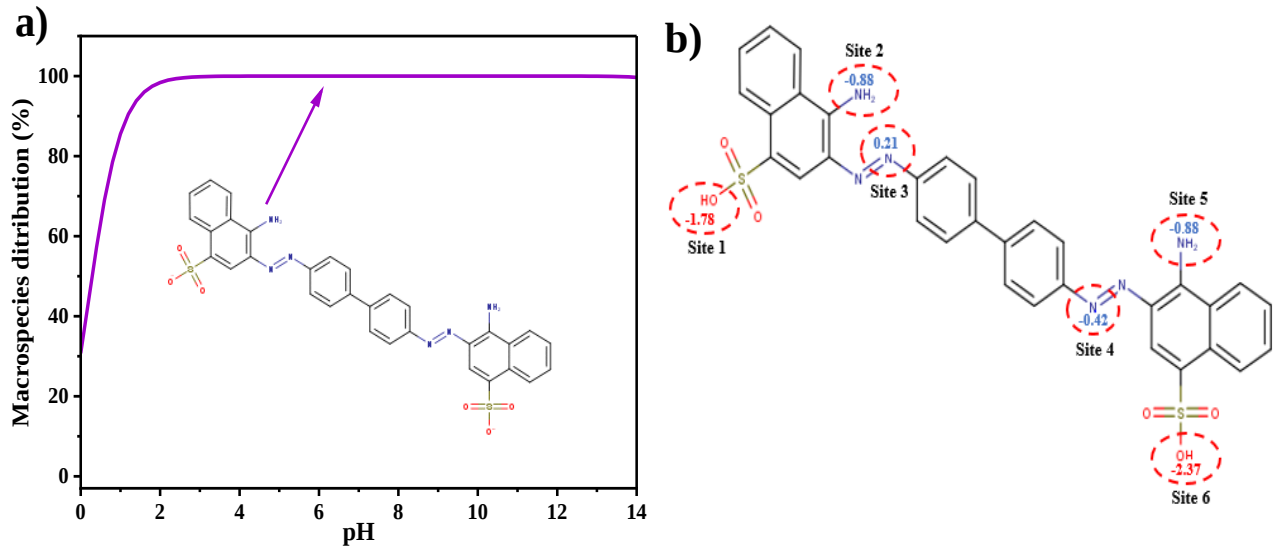

Fig. 7. a) Species distribution diagram of CR as a function of solution pH and the main species, b) The protonation sites of the CR molecule.

The adsorption removal efficiency of Congo Red on the $ZnMn_2O_4$ surface was investigated using a catalyst dosage of 0.8 g/L and an initial dye concentration of 20 mg/L under neutral pH conditions (**Fig. 8a**). The process exhibited rapid adsorption within the first 45 min, achieving a removal rate of 27.19% (6.79 mg/g), marking the first pseudo-steady state. A secondary increase followed, reaching 38.85% (9.71 mg/g) after 150 min and stabilizing at 38.98% by 180 min, indicating near-saturation and equilibrium.

The adsorption behavior was further analyzed by testing different initial CR dye concentrations, ranging from 10 to 30 ppm at room temperature, as shown in **Fig. 8b**. The removal efficiencies of CR decreased to 64.72%, 51.33%, 38.98%, 34.90% and 29.87% for concentrations of 10, 15, 20, 25, and 30 ppm after 180 min, respectively. At lower dye concentrations, the $ZnMn_2O_4$ adsorbent surface has ample active sites available for dye molecules, leading to higher removal rates. However, as the dye concentration increases, the adsorption sites become saturated, reducing the overall efficiency. This decline can be attributed to the competition among dye molecules for limited active sites on the adsorbent, resulting in lower percentages of dye being removed at higher concentrations.

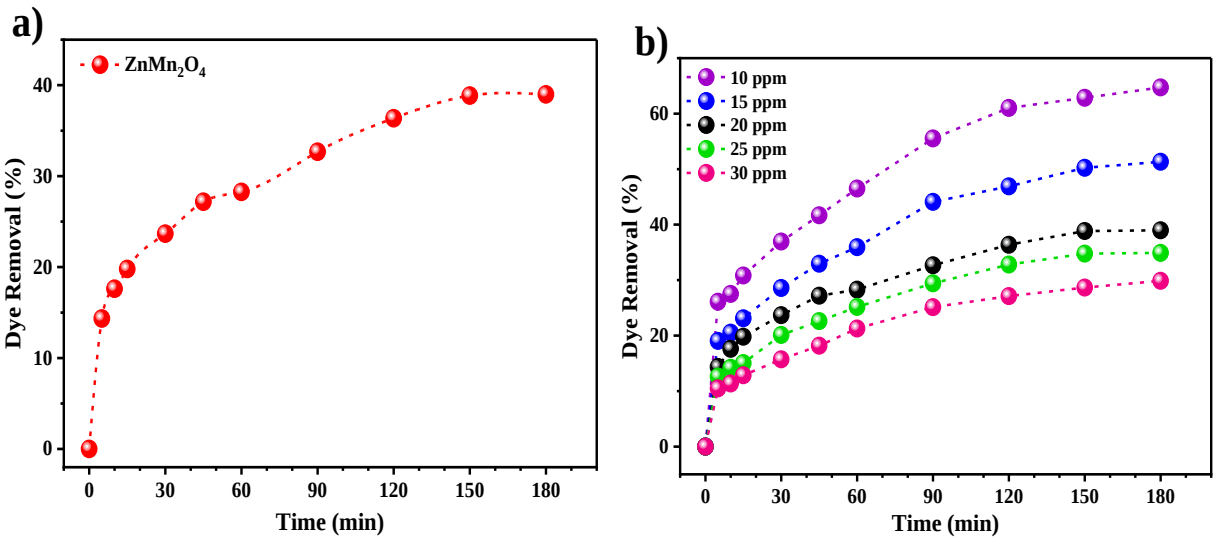

Fig. 8. a) The adsorption removal efficiency of Congo red onto $ZnMn_2O_4$ (catalyst dose: 0.8 g/L, C = 20 mg/L, pH = 6.1, T = 25 °C), b) Effect of concentration.

To elucidate the kinetics and mechanisms governing the adsorption process, the experimental data were analyzed using both the pseudo-first order and pseudo-second order models. These models provide critical insights into how adsorption capacity evolves over time and help

identify potential rate-limiting steps. Equations 16 and 17 correspond to the pseudo-first order and pseudo-second order kinetics [11], respectively.

$$\log(q_e - q(t)) = \log q_e - \frac{k_1}{2.303} t \quad (16)$$

$$\frac{t}{q(t)} = \frac{t}{q_e} + \left[\frac{1}{k_2 q_e^2}\right] \quad (17)$$

Where q(t) and q_e represent the amount of CR adsorbed at time (t) and at equilibrium, respectively. The constants k_1 and k_2 denote the rates of the pseudo-first order and pseudo-second order kinetics, respectively.

The linear fitting results for the experimental data on CR adsorption onto $ZnMn_2O_4$ are summarized in **Table 1**. The data align well with the pseudo-second order kinetic model, with a higher correlation coefficient (R^2 = 0.988) compared to the pseudo-first order model (R^2 = 0.837). Moreover, the equilibrium adsorption capacity calculated by the pseudo-second order model (10.611 mg/g) closely matches the experimental value (9.746 mg/g).

Table 1. Fitting parameters obtained using Eq. (15) and (16) for CR onto $ZnMn_2O_4$.

	Pseudo 1st order				**Pseudo 2nd order**			
Photocatalyst	**R^2**	**$q_{e,exp}$ (mg/g)**	**$q_{e,cal}$ (mg/g)**	**k_1 (min^{-1})**	**R^2**	**$q_{e,exp}$ (mg/g)**	**$q_{e,cal}$ (mg/g)**	**k_2 ($g.mg^{-1}.min^{-1}$)**
$ZnMn_2O_4$	0.837	9.746	9.702	$2.929\ 10^{-2}$	0.988	9.746	10.611	$4.784\ 10^{-3}$

Adsorption isotherm studies are essential for evaluating the capacity and surface properties of adsorbents. In this study, the adsorption isotherm of Congo red, at concentrations ranging from 10 to 30 mg/L, was evaluated using $ZnMn_2O_4$ at a dosage of 0.8 g/L and a temperature of 25 °C. According to IUPAC standards, the obtained isotherm was classified as type I.

A range of models is commonly employed to describe adsorption equilibrium. The Langmuir, Freundlich and Temkin models were applied to analyze the adsorption behavior of the $ZnMn_2O_4$ adsorbent, with the results presented in **Fig. S4** and **Table 2**. The Langmuir model provided the best fit, displaying the highest correlation coefficient (R^2 = 0.994). This model indicated a favorable adsorption process, with a separation factor (R_L) of 0.064 and an estimated monolayer adsorption capacity of 12.155 mg/g. Adsorption likely occurred on uniform sites, with no interactions between the adsorbed molecules, confirming that Congo red follows a monolayer adsorption mechanism on the $ZnMn_2O_4$ surface.

Table 2. Adsorption parameters of Langmuir, Freundlich and Temkin isotherm models.

Model	Parameters		R^2
Langmuir I	**q_m (mg/g)**	**K_L (L/mg)**	0.994
	12.155	0.482	
Freundlich	**K_F (mg/g).(mg/L)**	**1/n**	0.946
	6.543	0.176	
Temkin	**A_T (L/g)**	**b_T (J/mol)**	0.943
	35.061	1467.929	

3.5. Photocatalysis study

This study examined the photocatalytic efficiency of $ZnMn_2O_4$ in degrading CR under sunlight irradiation, using a dosage of 0.8 g/L across varying CR concentrations of 10, 15, 20, 25, and 30 mg/L, with results shown in **Fig. 9a**. CR exhibited high stability under natural pH conditions and solar exposure without any photocatalyst, achieving only 5.17% degradation after 180 min, indicating minimal photolysis. However, in the presence of $ZnMn_2O_4$, the degradation rate significantly increased, reaching 58.73%, 73.38%, 87.50%, 96.48%, and 99.97% for CR concentrations of 30, 25, 20, 15, and 10 mg/L, respectively, after 180 min.

The adsorption capacity is greater at lower concentrations, allowing for more active sites on the photocatalyst surface to interact with CR molecules. As the dye concentration rises, more molecules occupy these sites, which increases light absorption by the dye and reduces photon access to the photocatalyst surface. This diminished photon interaction results in a lower generation of reactive oxygen species (ROS), consequently decreasing the efficiency of dye removal [49, 50]. Therefore, CR photodegradation is more effective at reduced dye concentrations.

A pseudo-first order kinetic model was employed to assess the photocatalytic kinetics of CR degradation by the $ZnMn_2O_4$ photocatalyst, described by the following expression [51]:

$$Ln\left(\frac{C_0}{C_t}\right) = K_{app}\, t \qquad (18)$$

where C_0 and C_t represent the initial concentration and the concentration at time t, respectively, K_{app} denotes the pseudo-first order rate constant.

The photodegradation of CR using the $ZnMn_2O_4$ photocatalyst at various concentrations follows a pseudo-first order kinetic model, as shown in **Fig 9b**. The findings summarized in

Table 3 indicate that at a concentration of 20 ppm, the $ZnMn_2O_4$ exhibited a correlation coefficient (R^2) of 0.959, along with a rate constant (K_{app}) of 0.01074 min^{-1} and a half-life ($t_{1/2}$) of 64.5388 min.

The UV-vis absorption spectra were employed to monitor changes in CR absorption during its degradation by the $ZnMn_2O_4$ photocatalyst under sunlight irradiation, with a dosage of 0.8 g/L and an initial CR concentration of 20 ppm (**Fig. 9c**). A reduction in the CR dye solution's color intensity corresponded to a decrease in absorption within the visible spectrum. This decolorization is linked to the breakdown of the azo group responsible for the dye's coloration.

Table 3. Results of the pseudo-first order kinetic model fitting for the photocatalytic degradation of CR.

Initial concentration	**K_{app} (min^{-1})**	**$t_{1/2}$ (min)**	**R^2**
C_0 = 10 mg/L	0.04864	14.2505	0.982
C_0 = 15 mg/L	0.01666	41.6054	0.969
C_0 = 20 mg/L	0.01074	64.5388	0.959
C_0 = 25 mg/L	0.00669	103.6094	0. 952
C_0 = 30 mg/L	0.00451	153.6911	0.950

Fig. 9d illustrates the degradation of CR dye under solar light irradiation at different photocatalyst doses, ranging from 0.1 to 1 g/L. The results indicate that increasing the photocatalyst dosage enhances degradation efficiency, with $ZnMn_2O_4$ achieving an impressive 99.13% degradation of CR at a dosage of 1 g/L. Higher photocatalyst doses enhanced dye adsorption on the photocatalyst surface, increasing the availability of active sites and accelerating the reaction rate, which resulted in pronounced discoloration of the solution.

Photodegradation efficiency is strongly influenced by the pH of the dye solution, as it alters the surface charge of the photocatalyst [49]. This modification impacts the electrostatic interactions among dye molecules, the photocatalyst and reactive oxygen species (ROS), ultimately affecting the degradation process [52]. The influence of varying pH levels on the performance of synthesized $ZnMn_2O_4$ in degrading CR dye under 180 min of solar light exposure was examined (**Fig. 9e**). The natural pH of the CR solution was found to be 6.1, and the pH of the medium was adjusted between 2 and 10 by adding HCl or NaOH solutions. Photodegradation efficiency decreases as pH increases, reaching 51.02% at pH 10. This reduction in efficiency can be attributed to changes in the surface chemistry of $ZnMn_2O_4$ under

alkaline conditions. As the pH surpasses the point of zero charge (pH_{pzc}), the surface of $ZnMn_2O_4$ becomes negatively charged, increasing repulsion with the anionic CR dye and reducing adsorption efficiency.

Creating heterojunctions is a widely used strategy to enhance photocatalytic activity by improving charge separation and extending light absorption. To enhance the photocatalytic degradation efficiency of $ZnMn_2O_4$, a heterojunction with titanium dioxide (TiO_2) was formed, and the results are presented in **Fig. 9f**. The heterojunction was prepared via a physical mixing method, in which $ZnMn_2O_4$ and TiO_2 powders were thoroughly blended in appropriate proportions to achieve the desired mass ratio. The SEM images in **Figs. S5a** and **S5b** visually corroborate the successful formation of the $ZnMn_2O_4/TiO_2$ heterojunction. They clearly show the presence of both $ZnMn_2O_4$ and TiO_2 phases, exhibiting a uniform and homogeneous distribution and suggesting robust interfacial coupling between the two materials. TiO_2 was selected due to its well-established n-type semiconducting behavior, confirmed through a positive slope of the Mott-Schottky plot (**Fig. S5c**), with an E_{fb} of 300 mV/SCE.

Furthermore, the optical band gap of TiO_2 was first estimated from the inflection point of the first derivative of the diffuse reflectance spectrum plotted as a function of wavelength (**Fig. S6a**), yielding a value of 3.27 eV, which corresponds to an absorption edge (λ_0) at approximately 379 nm. To further confirm this result, Tauc plots were constructed based on the Kubelka–Munk function, F(R). For $n = 2$, which corresponds to an indirect allowed transition, the extrapolation of the linear region to the energy axis provided a band gap of 3.24 eV (**Fig. S6b**), in good agreement with the first derivative method. In contrast, the Tauc plot for $n = 1/2$, associated with a direct allowed transition (**Fig. S6c**), yielded a higher band gap value of 3.66 eV. This noticeable deviation from the values obtained using the indirect transition model and derivative analysis indicates that the optical transitions in the synthesized TiO_2 are of an indirect nature. The pHpzc was determined to be 5.61 using the pH drift method (**Fig. S6d**).

Using the various parameters compiled in Table S1, the energy band diagram for the p-$ZnMn_2O_4$/n-TiO_2 /electrolyte system was constructed and is shown in **Fig. S7a**. When the $ZnMn_2O_4/TiO_2$ heterojunction is exposed to solar irradiation, both semiconductor components simultaneously undergo photoexcitation. This process generates electron-hole pairs through the absorption of incident photons (hν), as described by Eq. 19 and Eq. 20:

$$ZnMn_2O_4 + h\nu \rightarrow ZnMn_2O_4\ (CB_{e^-} + VB_{h^+}) \quad (19)$$

$TiO_2 + h\nu \rightarrow TiO_2 (CB_{e^-} + VB_{h^+})$ (20)

The photoexcited electrons are able to migrate from $ZnMn_2O_4$-CB (-1.81 V) to that of TiO_2 (0.0 V), while the holes can move from TiO_2-VB (3.24 V) to the VB of $ZnMn_2O_4$ (0.16 V). This efficient separation of photogenerated charge carriers, enabled by the formation of a type-II semiconductor heterojunction, helps prevent electron-hole recombination.

In our system, the formation of $O_2^{\cdot -}$ or $^{\bullet}$OH radicals are unlikely, as the CB of TiO_2 is less negative than the redox potential of the $O_2/O_2^{\cdot -}$ (-0.56 V vs. SCE), and the VB of $ZnMn_2O_4$ is less positive than the redox potential of the $H_2O/^{\bullet}OH$ (1.73 V vs. SCE) [53]. Nevertheless, based on the band alignment of the $ZnMn_2O_4/TiO_2$ heterojunction, a direct Z-scheme charge transfer mechanism is proposed. In this configuration, electrons in the CB of TiO_2 recombine with holes in the VB of $ZnMn_2O_4$ at the interface. As a result, high-energy electrons are retained in the CB of $ZnMn_2O_4$ (exhibiting strong reducing ability), while high-energy holes accumulate in the VB of TiO_2 (offering strong oxidizing capability).

The electrons gathered in the conduction band of $ZnMn_2O_4$ reduce molecular oxygen (O_2) to generate superoxide radicals ($O_2^{\bullet -}$), which subsequently participate in further reactions leading to the formation of hydrogen peroxide (H_2O_2) and hydroxyl ions (OH^-).

$ZnMn_2O_4 + (CB_{e^-}) + O_2 \rightarrow ZnMn_2O_4 + O_2^{\bullet -}$ (21)

$2\ O_2^{\bullet -} + 2\ H_2O \rightarrow H_2O_2 + 2\ OH^- + O_2$ (22)

At the same time, the holes in the valence band of TiO_2 oxidize water molecules or hydroxide ions, leading to the formation of highly reactive hydroxyl radicals ($^{\bullet}OH$). These reactive oxygen species (ROS), especially $O_2^{\bullet -}$ and photogenerated holes (h^+), are primarily responsible for the oxidative degradation of Congo Red (CR).

$TiO_2 + (VB_{h^+}) + OH^- \rightarrow TiO_2 + {}^{\bullet}OH$ (23)

$TiO_2 + (VB_{h^+}) + H_2O \rightarrow TiO_2 + {}^{\bullet}OH + H^+$ (24)

Additionally, h^+ in $ZnMn_2O_4$ can contribute to OH^- generation.

$ZnMn_2O_4 + (VB_{h^+}) + H_2O \rightarrow ZnMn_2O_4 + H^+ + OH^-$ (25)

Congo Red molecules can be directly photoexcited under visible light and then undergo oxidation via interactions with photogenerated holes and reactive oxygen species (ROS).

CR Dye + hν → CR Dye* (26)

$$CR\ Dye^{*} + TiO_2 + (VB_{h+}) \rightarrow CR\ Dye^{\bullet+} + TiO_2 \quad (27)$$

The resulting CR $Dye^{\bullet+}$ radicals are further oxidized by ROS, leading to the generation of intermediate by-products and, ultimately, the complete mineralization of CR. This process underscores the high photocatalytic efficiency of the $ZnMn_2O_4/TiO_2$ heterojunction.

The resulting p-$ZnMn_2O_4$/n-TiO_2 heterojunction exhibited a notably high photodegradation rate, demonstrating accelerated activity within the initial minutes of solar exposure, independent of the heterojunction composition. Specifically, the p-$ZnMn_2O_4$/n-TiO_2 photocatalyst with a 75%/25% mass ratio achieved complete degradation of CR dye within 180 min.

The photoluminescence (PL) spectra of TiO_2, $ZnMn_2O_4$, and $ZnMn_2O_4/TiO_2$ were studied to evaluate their charge carrier recombination behavior (**Fig. S7b**). The results revealed that higher PL intensities correlate with increased electron-hole recombination, leading to lower photocatalytic activity. Notably, the $ZnMn_2O_4/TiO_2$ heterojunction exhibited significantly reduced PL emission peaks, indicating effective suppression of charge recombination. This suppression enhances charge separation and improves photocatalytic performance.

While the $ZnMn_2O_4$–TiO_2 heterojunction, with 25, 50 and 75 % content of $ZnMn_2O_4$, exhibited the highest photocatalytic performance among the tested compositions (Fig. S8), further increase in $ZnMn_2O_4$ content (i.e., 85% and 95%) led to a noticeable decline in degradation efficiency. This decline can be attributed to the reduced proportion of TiO_2, which plays a crucial role in promoting charge separation and suppressing the recombination of photogenerated electron–hole pairs. As the TiO_2 content diminishes, the system tends to behave similarly to pure $ZnMn_2O_4$, which exhibits lower photocatalytic activity. Conversely, at high TiO_2 loadings (85% and 95%), a similar decrease in activity is observed, likely due to the insufficient amount of $ZnMn_2O_4$, which is the primary light-absorbing component. These results highlight the importance of achieving a balanced ratio between the two components to optimize the synergistic effects of charge separation and light absorption.

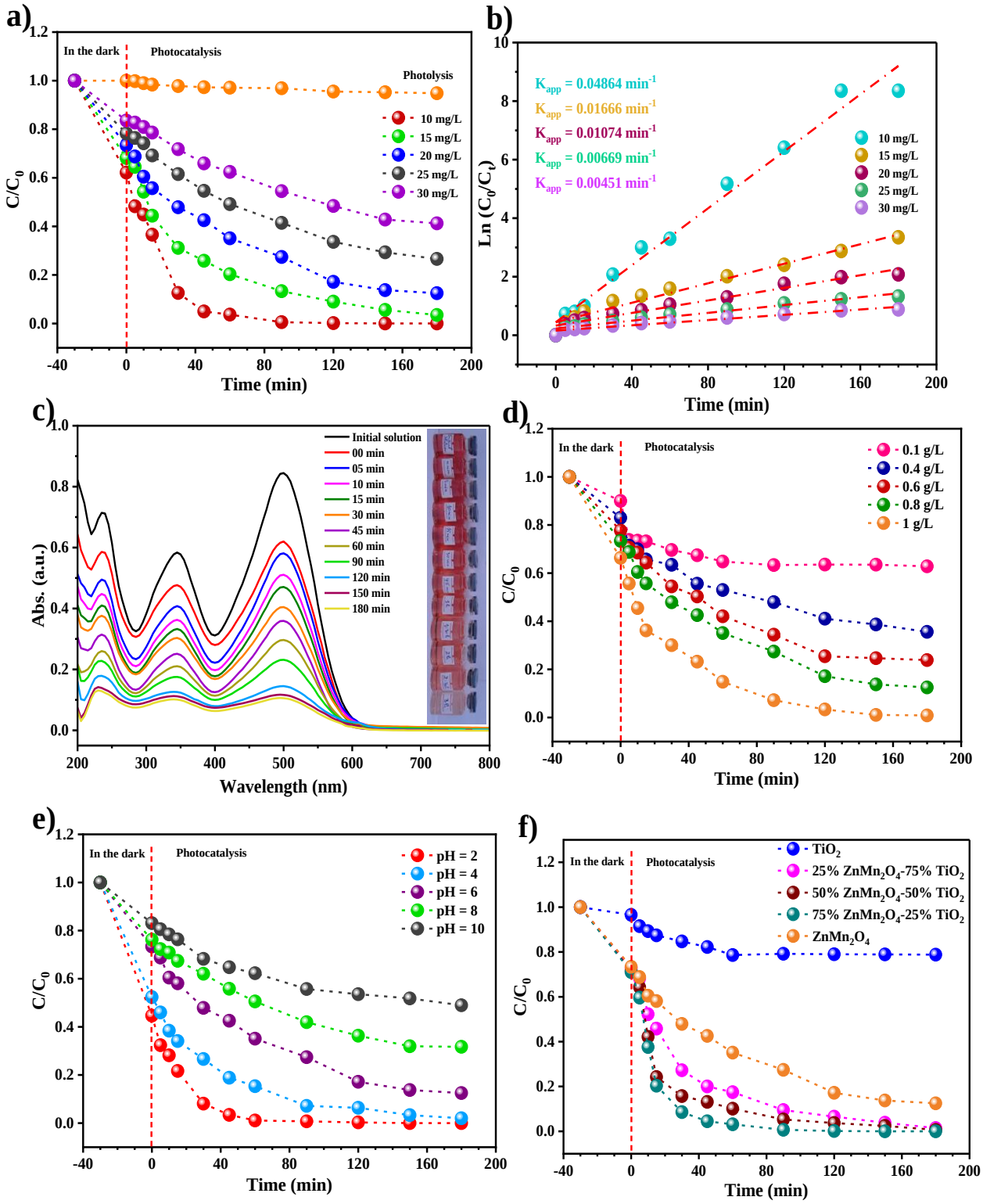

Fig. 9. a) Kinetics of the photocatalytic CR degradation on $ZnMn_2O_4$ photocatalysts (C_0 = 10, 15, 20, 25 and 30 mg/L, pH ~ 6.1, catalyst dose 0.8 g/L), b) Pseudo first order rate kinetics for photocatalytic degradation of CR, c) UV-Vis absorption spectra of the CR dye vs. irradiation time for $ZnMn_2O_4$ (C_0 = 20 mg/L), d) Effect of $ZnMn_2O_4$ photocatalyst dose, e) Effect of pH, f) Effect of the composition ratio.

Understanding the primary reactive species participating in the photocatalytic process is essential to uncover the degradation mechanism. Therefore, selective scavengers were introduced, each targeting a specific species. Ascorbic acid to quench superoxide radicals ($O_2^{\bullet-}$), silver nitrate ($AgNO_3$) to trap electrons (e^-), isopropanol (IPA) to capture hydroxyl radicals ($^{\bullet}OH$), while disodium EDTA (EDTA-2Na) and potassium iodide (KI) to scavenge holes (h^+).

The effect of scavengers on CR dye degradation using $ZnMn_2O_4$ is depicted in **Fig. 10a**. The presence of ascorbic acid slightly enhances the degradation efficiency to 92.69%, compared to 87.50% without scavengers, suggesting that superoxide radicals ($O_2^{\bullet-}$) play a limited role. In contrast, the addition of EDTA-2Na and KI significantly reduces the efficiency to 71.60% and 59.87%, respectively, confirming that holes (h^+) are the primary contributors to CR degradation. Furthermore, the introduction of isopropanol decreases the degradation rate to 58.09%, indicating the involvement of hydroxyl radicals ($^{\bullet}OH$), whose impact is more pronounced than that of holes (h^+). The use of $AgNO_3$ as an electron (e^-) scavenger increases the degradation efficiency to 97.46%. These findings indicate that holes (h^+) and hydroxyl radicals ($^{\bullet}OH$) are the primary active species in the photocatalytic degradation of CR on the $ZnMn_2O_4$ photocatalyst under sunlight.

To investigate the influence of hydrogen peroxide (H_2O_2) on the photocatalytic activity of $ZnMn_2O_4$, experiments were conducted using H_2O_2 concentrations of 3, 6, 10, 15, and 20 mmol/L (**Fig. 10b**). In the absence of H_2O_2, $ZnMn_2O_4$ achieved an 87.50% degradation rate of CR after 180 min of solar exposure. The addition of H_2O_2 markedly increased degradation efficiency, with the highest observed rate reaching 97.47% at 10 mmol/L. This enhancement is attributed to a higher yield of hydroxyl radicals and the inhibition of electron-hole recombination, with H_2O_2 acting as a sacrificial electron acceptor and producing reactive oxygen species. However, at higher concentrations, the efficiency slightly decreased, with degradation rates of 83.74% and 79.48% at 15 and 20 mmol/L, respectively.

The recyclability of $ZnMn_2O_4$ was evaluated by analyzing its structural stability through XRD before and after four successive photocatalytic cycles (**Fig. 10c**). The XRD patterns revealed no significant changes in peak positions or the formation of new phases, confirming that the crystal structure of the material remained intact. This stability underscores the robustness of $ZnMn_2O_4$, ensuring consistent performance and supporting its suitability for repeated photocatalytic applications.

To evaluate the reusability of $ZnMn_2O_4$, photocatalytic degradation experiments were performed over four consecutive cycles (**Fig. 10d**). A minor decline of 9% in degradation efficiency was observed, likely due to surface coverage by residual degradation products and photocatalyst mass loss during its collection.

The photocatalytic performance of $ZnMn_2O_4$ for Congo Red (CR) was evaluated and compared to previously reported results for Rhodamine B (RhB), as illustrated in **Fig. 10e**. For RhB (10 ppm), the degradation efficiency was limited to 25.96% after 180 min of solar irradiation, using a photocatalyst dosage of 1 g/L [24]. This lower performance is attributed to electrostatic repulsion between the positively charged RhB molecules and the photocatalyst surface, which hindered adsorption and reactive interactions. In contrast, CR (20 ppm) exhibited a significantly higher degradation efficiency of 87.50% under the same irradiation time, despite using a lower photocatalyst dose (0.8 g/L). This enhanced performance can be explained by the strong electrostatic attraction between the anionic CR molecules and the $ZnMn_2O_4$ surface, which facilitated better adsorption and more efficient charge transfer.

To further contextualize the photocatalytic efficiency of $ZnMn_2O_4$, a comparative summary is provided in **Table 4**, compiling recent reports on Congo Red degradation using a range of semiconductor photocatalysts under different irradiation conditions. $ZnMn_2O_4$ achieved a degradation efficiency of 87.50% under solar light within 180 min, using a moderate catalyst dosage (0.8 g/L) and a relatively high initial dye concentration (20 mg/L). In contrast, several systems in the literature required more intense light sources (UV or visible), higher catalyst loadings, or dopant modifications to attain comparable or lower efficiencies. This remarkable performance demonstrates the intrinsic photocatalytic activity of $ZnMn_2O_4$ and underscores its potential as a cost-effective, sustainable, and standalone photocatalyst for solar-driven wastewater remediation, without reliance on complex heterostructures or additional chemical modifications.

Table 4. Comparison of photocatalytic degradation performance for Congo Red dye using various photocatalysts under different experimental conditions.

Photocatalyst	Light source	Conditions	Degradation Efficiency (%)	Ref.
$ZnCo_2O_4$	Solar light	C_0 = 10 mg/L t = 2 h r = 0.8 g/L	61%	[23]
$CoFe_2O_4$	UV light	C_0 = 10 mg/L t = 90 min r = 0.7 g/L	84%	[54]
$CuBi_2O_4$	Visible light	C_0 = 20 mg/L t = 70 min r = 1 g/L	46%	[55]
$Ca_{0.1}Cu_{0.95}Bi_2O_4$	Visible light	C_0 = 20 mg/L t = 70 min r = 1 g/L	82%	[55]
$Ni_{0.6}Cu_{0.4}Fe_2O_4$	Visible light	C_0 = 20 mg/L t = 100 min r = 1 g/L	63.18%	[22]
WO_3	UV light	C_0 = 10 mg/L t = 5 h r = 1.67 g/L	74.3%	[56]
Ag-MgO	UV light	C_0 = 10 mg/L t = 2 h r = 0.2 g/L	80%	[57]
ZnO	UV-Visible light	C_0 = 10 mg/L t = 100 min r = 0.4 g/L	57.6%	[21]
Cu_2O	Solar light	C_0 = 10 mg/L t = 2 h r = 1 g/L	65.66%	[58]
$ZnMn_2O_4$	Solar light	C_0 = 20 mg/L t = 3 h r = 0.8 g/L	87.50%	This work

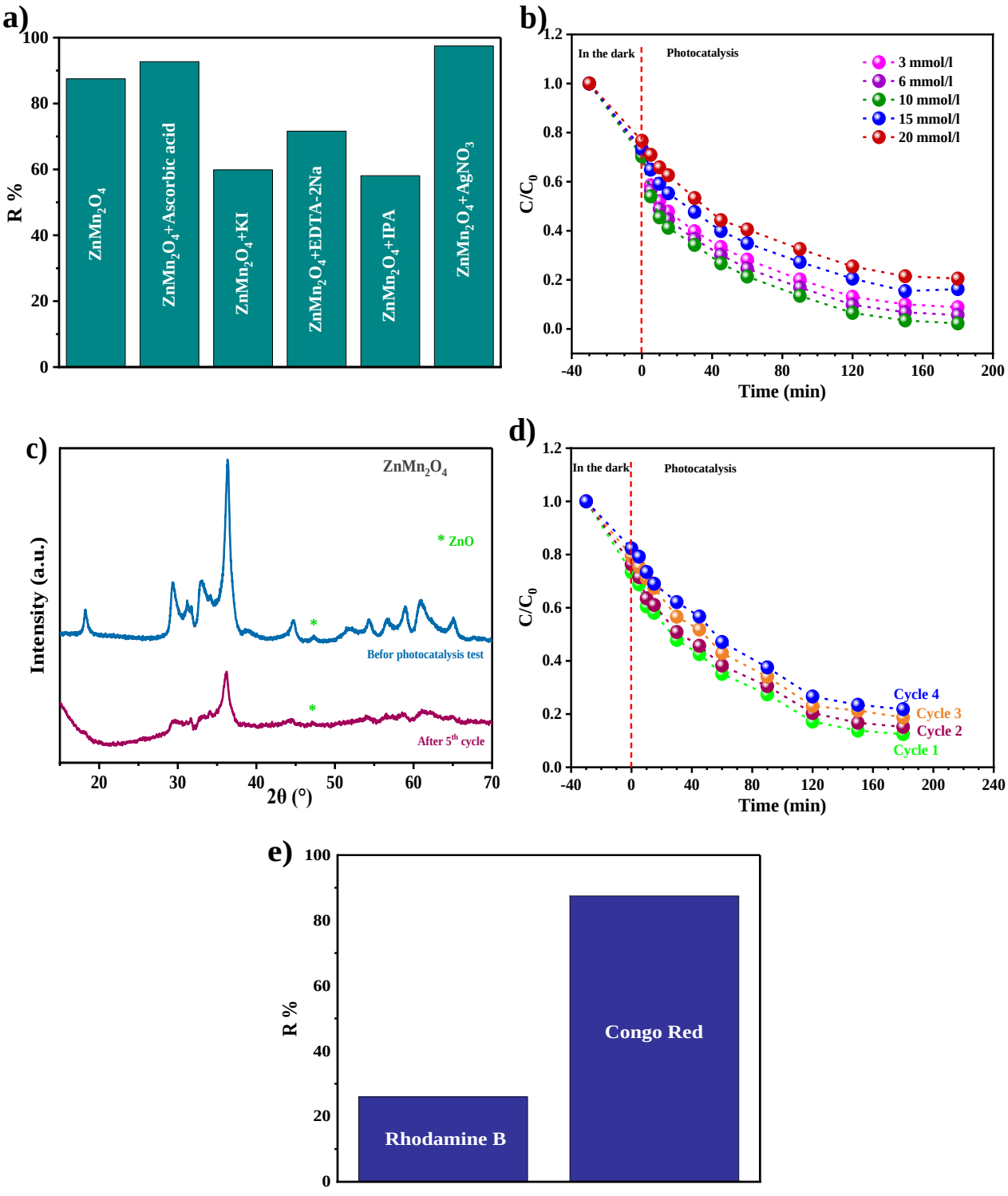

Fig. 10. a) Effect of scavengers on the CR photodegradation, b) Effect of H_2O_2 addition, c) XRD patterns of $ZnMn_2O_4$ photocatalyst before and after recyclability, d) Cycling degradation of CR over $ZnMn_2O_4$, e) Degradation efficiency of RhB and CR using $ZnMn_2O_4$.

3.6. Theoretical Study

3.6.1. Quantum chemical studies of Congo Red using DFT

Density Functional Theory, a widely used computational approach for investigating electronic structures and reaction mechanisms, was employed to elucidate the degradation pathways of Congo Red and its intermediates. The optimized molecular geometry of CR was obtained using the DFT/Dmol^3 method with the Generalized Gradient Approximation (GGA) Perdew–Burke–Ernzerhof (PBE) functional in an aqueous solvent (H_2O).

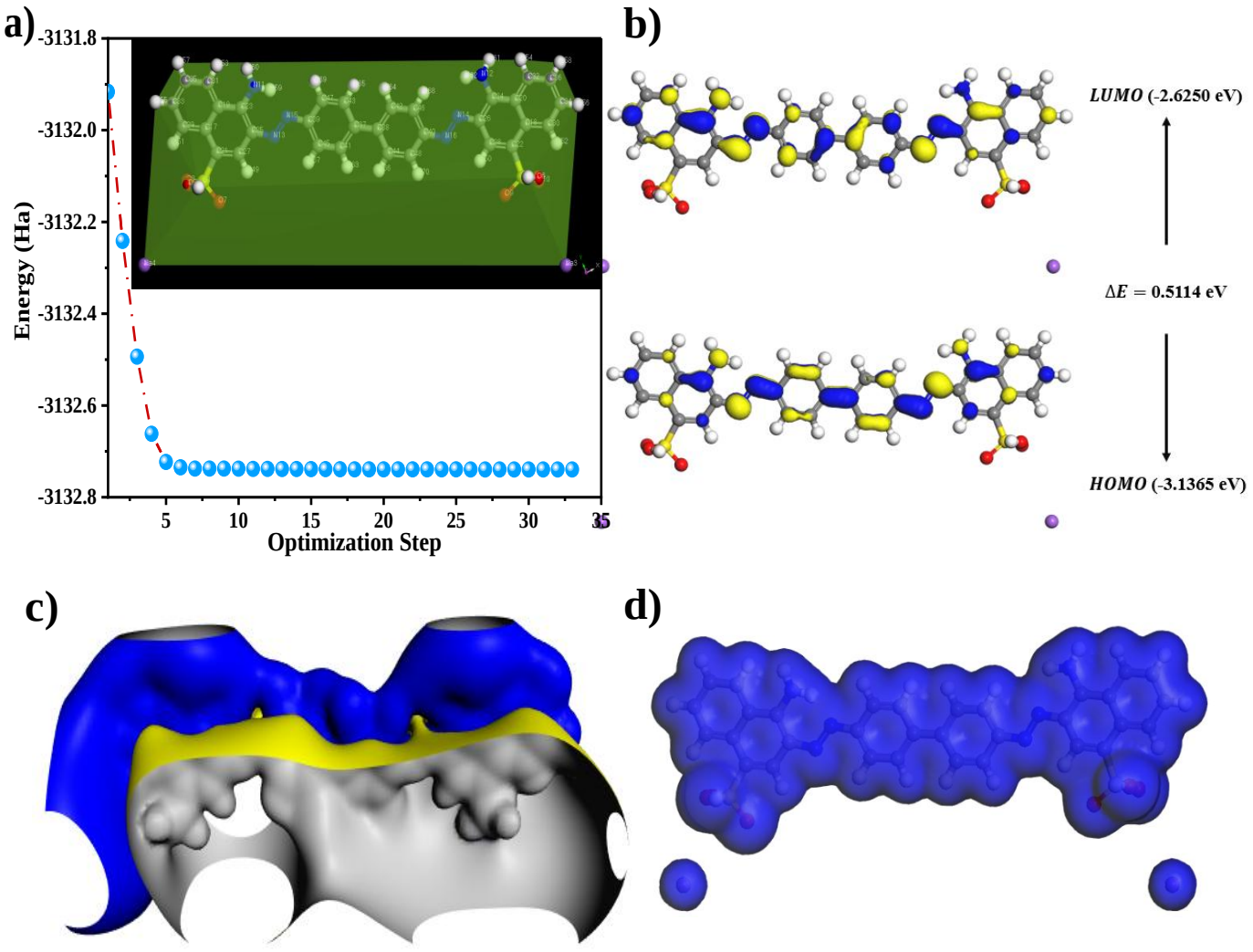

Fig. 11. a) Optimized molecular geometry of the CR molecule obtained using DFT/Dmol^3 method with the GGA/PBE functional. b) Frontier molecular orbitals representing the HOMO and LUMO. c) Molecular Electrostatic Potential Surface (MESP) illustrating charge distribution. d) Electron density distribution of the CR.

The energy profile illustrated in **Fig. 11a** exhibits a continuous decrease toward the lowest energy state. Beginning with an initial energy of -3131.91652 Ha, the system undergoes

significant geometric rearrangements, leading to a sharp energy reduction to -3132.66179 Ha by the fourth optimization step. As the optimization process progresses, the rate of energy reductions decreases considerably, with only minor variations from -3132.72307 Ha at step 5 to -3132.73957 Ha at step 33. The minimal energy fluctuation observed in the final steps confirms that the system has reached an optimized molecular geometry, demonstrating the robustness and reliability of the computational approach employed.

The three-dimensional (3D) representations of the frontier molecular orbitals, Highest Occupied Molecular Orbital (HOMO) and Lowest Unoccupied Molecular Orbital (LUMO), are presented in **Fig. 11b**. The electron density distribution in both orbitals is nearly uniform and is predominantly delocalized over the two benzene-azo (C_6H_4-N=N-) groups, while, excluding the sulfonate ($-SO_3^-$) functional groups and sodium ions (Na^+). This charge distribution highlights the regions most favorable for electrophilic and nucleophilic attacks, providing valuable insights into the molecule's reactivity.

The ESP map illustrates variations in electrostatic potential across the molecular surface, providing valuable insight into the chemical reactivity of the compound. This approach enables the identification of electrophilic and nucleophilic sites, which are essential for understanding intermolecular interactions and reaction mechanisms. As depicted in **Fig. 11c**, regions of high positive potential predominantly cover the molecule, except at the SO_3 functional group, indicating susceptibility to nucleophilic attack. In contrast, the SO_3 group exhibits a pronounced negative potential, identifying it as a preferred electrophilic site for molecular interactions.

The total electron density map offers deeper insights into the electronic structure of the compound, highlighting electron-rich and electron-deficient regions. As illustrated in **Fig. 11d**, the total electron density map of the CR dye displays electron-depleted zones in blue, which may enhance interactions with semiconductors and facilitate processes such as adsorption or photocatalytic degradation.

Table 5 presents a summary of the HOMO and LUMO energies of the CR dye, which determine its electron-donating (E_{HOMO} = -3.1365 eV) and electron-accepting (E_{LUMO} = -2.6250 eV) characteristics. The higher LUMO energy relative to HOMO signifies an increased propensity for electron acceptance over donation, providing insights into donor-acceptor interactions at the semiconductor interface. The energy gap (ΔE_{gap} = 0.5114 eV), a fundamental parameter governing molecular reactivity, classifies the CR dye as a soft molecule, characterized by low stability and high reactivity due to its narrow ΔE gap. This small energy gap is strongly

correlated with enhanced adsorption at the semiconductor surface, emphasizing the dye's potential for applications requiring efficient interfacial charge transfer.

The chemical potential (μ) represents the change in free energy associated with the addition of atoms of a given species. For CR, the computed value of -2.8808 eV indicates significant electron affinity. Such a negative chemical potential typically implies molecular stability and a strong tendency to accept electrons, whereas higher chemical potentials are generally correlated with enhanced reactivity and a greater susceptibility to degradation under light exposure.

The chemical softness characterizes a molecule's ability to exchange electrons with its surroundings. Molecules exhibiting high softness and low hardness demonstrate enhanced reactivity, as they can effectively polarize or redistribute electron density in response to external stimuli. This property plays a fundamental role in electron transfer, adsorption, and nucleophilic or electrophilic interactions. The values presented in **Table 5** indicate that the CR dye possesses pronounced softness, with a value of 3.9101 eV^{-1}, significantly exceeding its hardness of 0.2557 eV. This marked disparity classifies CR it as a soft molecule, highlighting its strong potential for chemical interactions.

The electrophilicity index (ω) is a fundamental quantitative descriptor used to assess a molecule's electron-accepting capacity of a molecule, offering critical insights into its reactivity, stability and chemical behavior. Molecules with a high electrophilicity exhibit strong electrophilic tendencies, readily attracting electrons from nucleophiles and demonstrating heightened reactivity [59]. Conversely, species with lower electrophilicity values display reduced electron-accepting capacity, indicating weaker electrophilic behavior.

In this context, the electrophilicity index of CR dye is notably high (16.2250 eV), underscoring its strong electron-accepting potential and reactivity in chemical processes.

The Fukui functions (f^+, f^-, f^0) of the CR molecule were analyzed, with results presented in **Fig. 12a**. These functions serve as essential descriptors of molecular reactivity, enabling the identification of specific atomic sites that govern electron transfer processes. The f^+ function, which characterizes regions susceptible to nucleophilic attack, exhibits significant positive regions at N16 (0.051), N15 (0.042), N13 (0.039), and N14 (0.035), indicating a high propensity for electron acceptance. In contrast, the f^- function, which identifies sites favorable for electrophilic interactions, is marked by pronounced negative values at N14 (0.049), N13 (0.048), N16 (0.040), and N15 (0.030), signifying their tendency to donate electrons. Furthermore, the f^0 function, which evaluates susceptibility to free radical attacks, highlights

the most reactive atomic sites at N16 (0.045), N13 (0.044), N14 (0.042), and N15 (0.036), providing deeper insights into the molecule's chemical behavior and potential interaction mechanisms.

Table 5. Quantum chemical parameters for the CR molecule Computed using DFT/Dmol^3 with GGA/PBE in an aqueous solvent (H_2O).

Descriptor	Formula	Value (eV)
Ionization potential(I)	$I = -E_{HOMO}$	3.1365
Electron affinity(A)	$A = -E_{LUMO}$	2.6250
Energy Gap (ΔE)	$\Delta E = E_{LUMO} - E_{HOMO}$	0.5114
Chemical potential (μ)	$\mu = -\frac{(I + A)}{2}$	-2.8808
Electronegativity (χ)	$\chi = \frac{(I + A)}{2}$	2.8808
Hardness (σ)	$\eta = \frac{I - A}{2}$	0.2557
Softness	$\sigma = \frac{1}{\eta}$	3.9101
Electrophilicity index (ω)	$\omega = \frac{\mu^2}{2\eta}$	16.2250

The reactivity of the CR dye was analyzed using the dual descriptor (f_k^2), local softness ($\Delta\sigma_k$), and local philicity ($\Delta\omega_k$), as illustrated in **Fig. 12b**. A positive f_k^2 value at N15 (0.012) and N16 (0.011) indicates that these sites exhibit enhanced reactivity toward nucleophiles. Likewise, elevated local softness values ($\Delta\sigma_k > 0$) at N15 (0.0469212), N16 (0.0430111), C33 (0.0273707) and C31 (0.0234606) further highlight their pronounced susceptibility to nucleophilic interactions, reinforcing their role in electron transfer processes and molecular reactivity. Moreover, local electrophilicity is concentrated at key reactive sites, including N15 (0.194700), N16 (0.178475), C33 (0.113575), C31 (0.097350), C29 (0.081125), C45 (0.081125) and C46 (0.081125). These findings identify regions susceptible to nucleophilic attack, offering deeper insights into the dye's electron exchange dynamics during semiconductor interactions.

The frontier electron density (FED) distribution and natural population analysis for the CR molecule, computed using DFT with the 6-31++G(d, p) basis set in Gaussian 16W software, are presented in **Fig. 12c**. The FED values facilitate the identification of the atoms most

susceptible to radical attack, as atoms with higher (FED^2_{HOMO} + FED^2_{LUMO}) values exhibit increased reactivity toward hydroxyl radicals (•OH) [60, 61]. The highest FED values are observed for atoms O6 (1.2853) and O7 (1.2857), indicating a strong propensity for electrophilic attack. However, due to the absence of a bonded hydrogen on O7, hydrogen abstraction is expected to occur at alternative sites. Among these, O5, which carries a notably negative partial charge (-0.95068), is identified as a likely target for •OH-induced hydrogen abstraction.

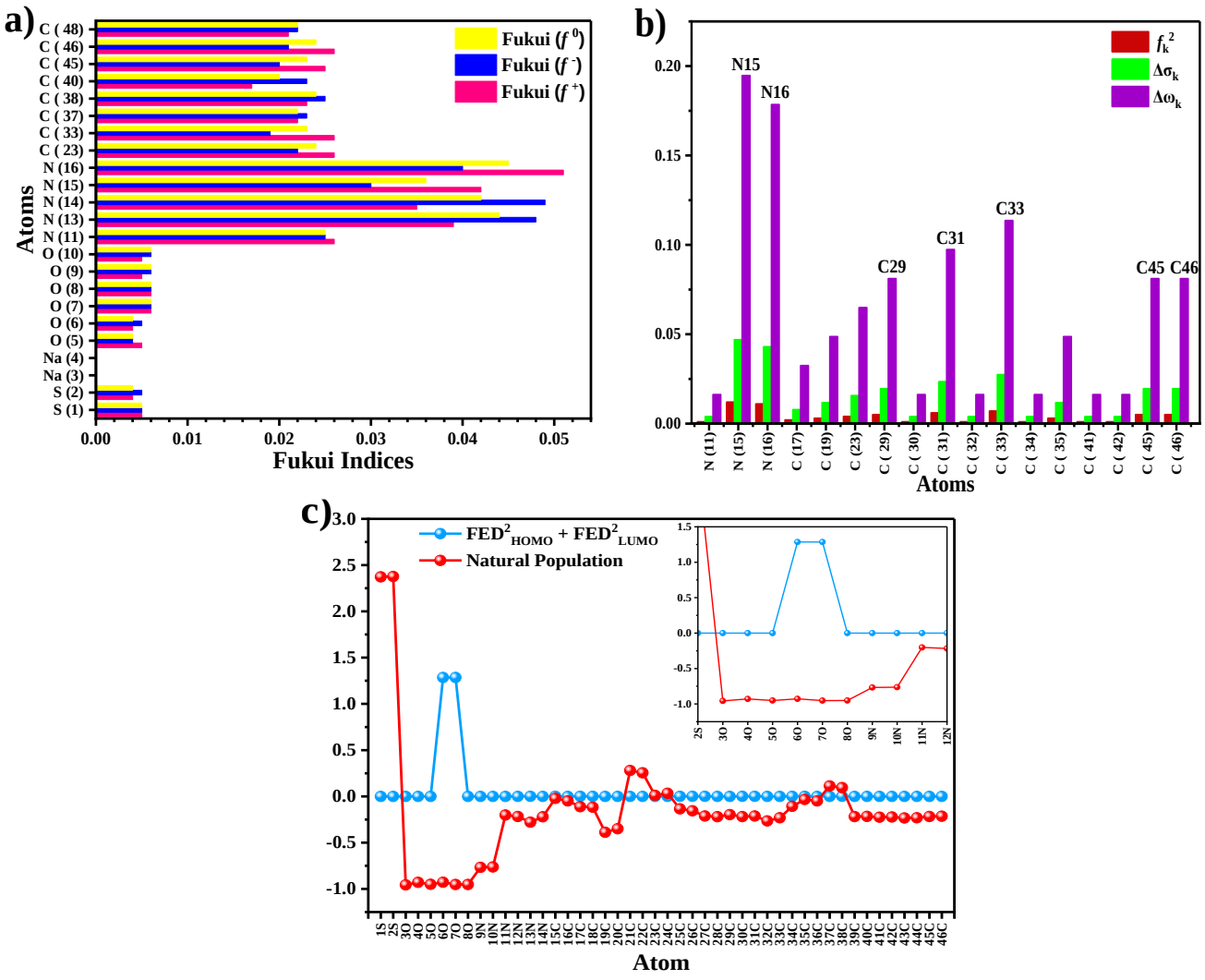

Fig. 12. a) Fukui functions (f^+, f^-, f^0) identifying reactive molecular sites of the Congo Red (CR) molecule. b) Local dual descriptors (f_k^2, $\Delta\sigma_k$, $\Delta\omega_k$) mapping site-specific reactivity. c) Frontier electron density (FED) distribution and natural population analysis, characterizing atomic charge distribution.

3.6.2. Monte Carlo and Molecular Dynamics simulations

Based on the experimental conditions, the initial concentrations were set to 20 ppm for Congo Red (CR) and 10 ppm for Rhodamine B (RhB). To ensure an accurate representation of their adsorption behaviors, two CR molecules and one RhB molecule were introduced into their respective simulation systems. Each dye was independently simulated using both Monte Carlo and Molecular Dynamics approaches.

Fig. 13a and **b** illustrate the energy profiles corresponding to the adsorption of CR and RhB on the $ZnMn_2O_4$ surface in aqueous media, as determined through Monte Carlo simulations using the Locator model. The total and electrostatic energy curves exhibit marked fluctuations, indicative of strong and dynamic interactions between the dyes and the substrate.

The periodic, sharp energy drops correspond to successive adsorption-desorption events, followed by subsequent restabilization of the systems. The close alignment between total and electrostatic energy curves underscores the dominant role of electrostatic interactions in stabilizing both dyes. Conversely, the van der Waals energy remains nearly constant and close to zero, suggesting a minimal contribution from dispersion forces.

The average total energy profile reveals an initial steep decline, followed by well-defined plateaus, reflecting gradual stabilization of the dye-surface systems. Moreover, the intramolecular energy remains constant throughout, confirming the absence of significant structural distortions during adsorption. Notably, CR exhibits deeper energy minima and more pronounced fluctuations than RhB, indicating a stronger affinity and a more dynamic adsorption behavior on the $ZnMn_2O_4$ surface.

The adsorption configurations of CR and RhB on the $ZnMn_2O_4$/200 H_2O surface are illustrated in **Fig. 13c, d**, with corresponding results detailed in **Table 6**. MC simulations reveal that CR exhibits a higher adsorption energy (-16147.31 kcal/mol) than RhB (-15952.83 kcal/mol), indicating a stronger overall interaction with the surface. This trend is further supported by the rigid adsorption energies, where CR reaches -18695.60 kcal/mol, slightly surpassing that of RhB (-18316.78 kcal/mol). Additionally, the deformation energies obtained for CR (2548.29 kcal/mol) and RhB (2363.95 kcal/mol) indicate that both dyes undergo moderate conformational adjustments upon adsorption.

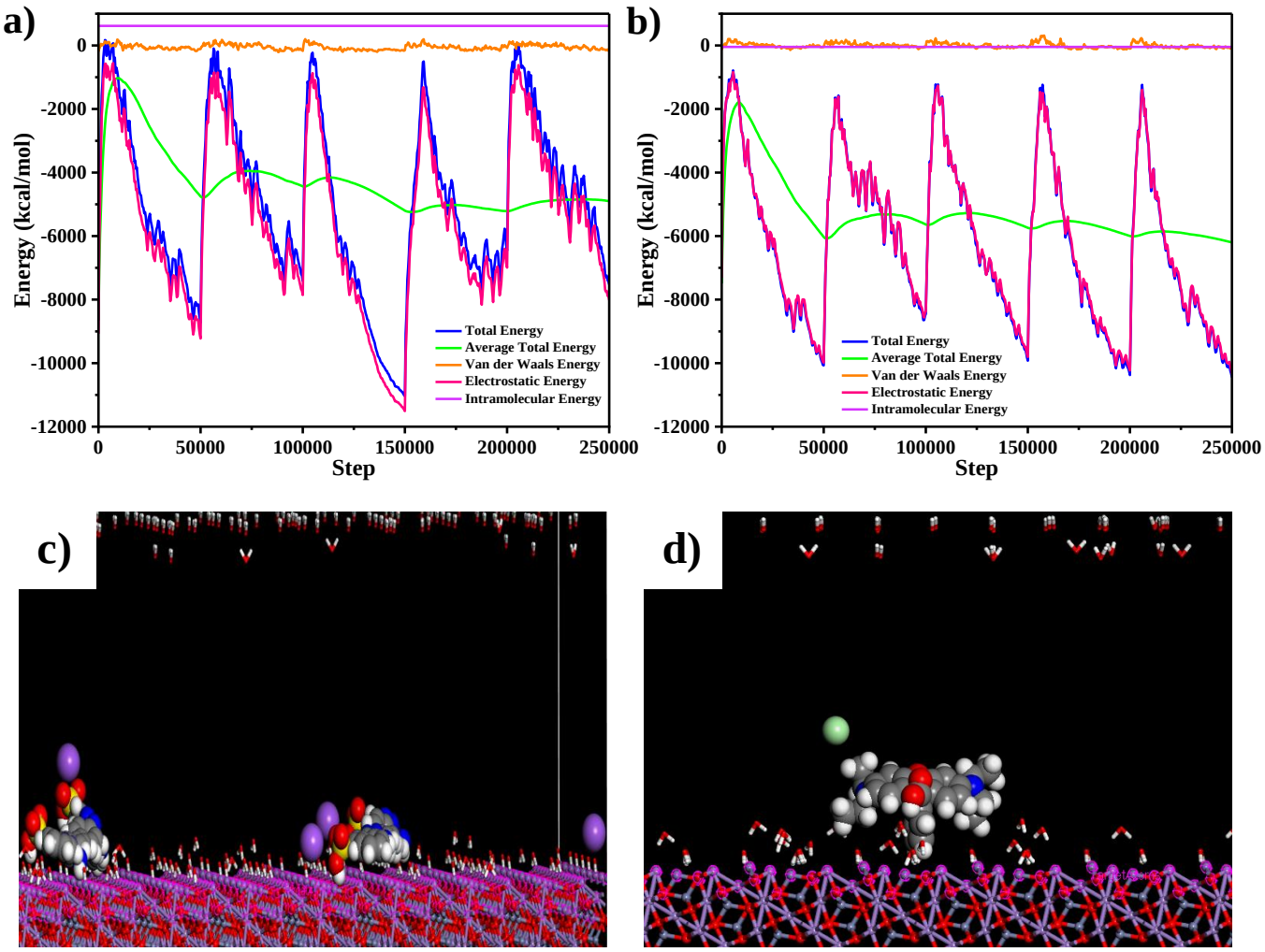

Fig. 13. (a, b) Total adsorption energy profiles of Congo Red (CR) and Rhodamine B (RhB) on the $ZnMn_2O_4$/200 H_2O surface, obtained using Locator model calculations. (c, d) Side views illustrating the adsorption configurations of CR and RhB on the $ZnMn_2O_4$/200 H_2O surface.

Table 6. Outputs and descriptors obtained from Monte Carlo simulation for Congo Red and Rhodamine B adsorption on the $ZnMn_2O_4$/200 H_2O surface.

Compounds	Adsorption energy (kcal/mol)	Rigid adsorption energy (kcal/mol)	Deformation energy (kcal/mol)	dE_{ad} / dN_i (kcal/mol)
2 CR/$ZnMn_2O_4$/200H_2O	-16147.31	-18695.60	2548.292	-302.619
RhB/$ZnMn_2O_4$/200H_2O	-15952.83	-18316.78	2363.950	-635.363

The interaction energy ($E_{Interaction}$) and binding energy ($E_{Binding}$) for CR and RhB adsorbed on the $ZnMn_2O_4$ surface in an aqueous environment, as obtained via molecular dynamics simulations, are summarized in **Table 7**. The negative values of $E_{Interaction}$ indicate enhanced system stability, arising from stronger dye-surface interactions. Conversely, the positive values of $E_{Binding}$ signify favorable adsorption behavior, characterized by a strong affinity between the pollutant and the semiconductor interface. Among the two dyes, CR exhibits a more negative interaction energy ($E_{Interaction}$ = -3256.52 kcal/mol) and a higher binding energy ($E_{Binding}$ = 3256.52 kcal/mol) compared to RhB, indicating stronger interfacial interactions and a greater adsorption affinity. This enhanced interaction is likely driven by hydrogen bonding, which appears to play a more significant role than dispersion forces. These findings are consistent with the Monte Carlo simulation results, further corroborating the greater adsorption capacity and higher stability of CR on the $ZnMn_2O_4$ surface.

Table 7. Output descriptors calculated from molecular dynamics simulations for adsorption on the $ZnMn_2O_4$ surface.

Compound	$E_{Interaction}$ (kcal/mol)	$E_{Binding}$ (kcal/mol)
2 CR/$ZnMn_2O_4$/200H_2O	-3256.52	3256.52
RhB/$ZnMn_2O_4$/200H_2O	-3023.12	3023.12

3.6.3. Toxicity assessment of the degradation intermediates

The toxicity of Congo Red and its degradation intermediates was evaluated based on degradation pathways adopted from the study by Shah et al. [62], which proposed hydroxyl radical ($^{\bullet}OH$) driven mechanisms considering fragmentation patterns and the structural characteristics of the resulting species. These intermediates were identified through ultra-performance liquid chromatography coupled with tandem mass spectrometry (UPLC-MS/MS), and their structures were elucidated via mass spectral analysis. Five major intermediates were reported, primarily formed through oxidation reactions, electron transfer, and bond cleavage processes.

According to their findings, CR undergoes degradation via two principal pathways.

- Pathway I: Hydroxyl radicals ($^{\bullet}OH$) initiates electron transfer at the sulfonic acid group ($-SO_3^-$), generating a sulfur-centered radical cation. This intermediate undergoes oxidation to sulfate, leading to the formation of intermediate A (m/z = 492). A then

undergoes substitution with an amino group, resulting to in ammonia release and formation of intermediate B (m/z = 462). Subsequent $^{\bullet}OH$ attack at the nitrogen atom bonded to the biphenyl structure induces bond cleavage, yielding intermediate C (m/z = 307).

- Pathway II: ($^{\bullet}OH$) radicals target the nitrogen atom attached to a smaller fragment containing $-NH_2$ and $-SO_3^-$ groups, initiating electron transfer and bond scission. This leads to the formation of intermediates D (m/z = 401) and E (m/z = 222) via nitrogen loss. Additionally, intermediate D may undergo further $^{\bullet}OH$-driven oxidation and substitution reactions, converting into intermediate C.
- Although the degradation mechanisms and transformation pathways of Congo Red (CR) have been extensively investigated, the toxicological behavior of CR and its intermediates remains insufficiently characterized. To date, only one study [63] has evaluated their toxicity using the Toxicity Estimation Software Tool (TEST). In the present study, the toxicity profiles of CR and its degradation products were predicted using TEST, with the results presented in **Fig. 14**.

The acute toxicity was assessed using the Daphnia magna LC_{50} (48 h), which represents the concentration required to induce 50% mortality in a Daphnia magna population within 48 h. As illustrated in **Fig. 14a**, intermediates A (LC_{50} =7.82) and B (LC_{50} =7.59) exhibited higher LC_{50} values than CR (LC_{50} = 6.60), indicating greater toxicity relative to the parent compound. Conversely, intermediates C (LC_{50} = 6.18), D (LC_{50} = 5.71), and E (LC_{50} = 4.26) displayed lower LC_{50} values, suggesting reduced toxicity. These findings imply a progressive decline in acute toxicity throughout the reaction process, with a more than 200-fold decrease compared to the initial CR toxicity level.

The oral rat LD_{50} (50% lethal dose) was utilized to estimate the acute mammalian toxicity of the intermediates (**Fig. 14b**). Intermediates A and B were labeled as N/A, likely due to instability that precludes accurate prediction. CR exhibited an LD_{50} of 2.20 ($-\log_{10}$ mol/kg), while intermediates C, D, and E showed values of 2.39, 1.79, and 1.53, respectively. Based on these results, intermediate E demonstrated less toxicity than the parent CR dye.

The bioconcentration factor (BCF) was utilized to assess the extent to which a compound accumulates within an organism relative to its environment (**Fig. 14c**). CR dye exhibited a low BCF of 0.36, suggesting rapid metabolism or elimination following uptake. In contrast, intermediate C demonstrated the highest accumulation potential, with a BCF of 2.04, indicating a greater likelihood of retention within biological systems.

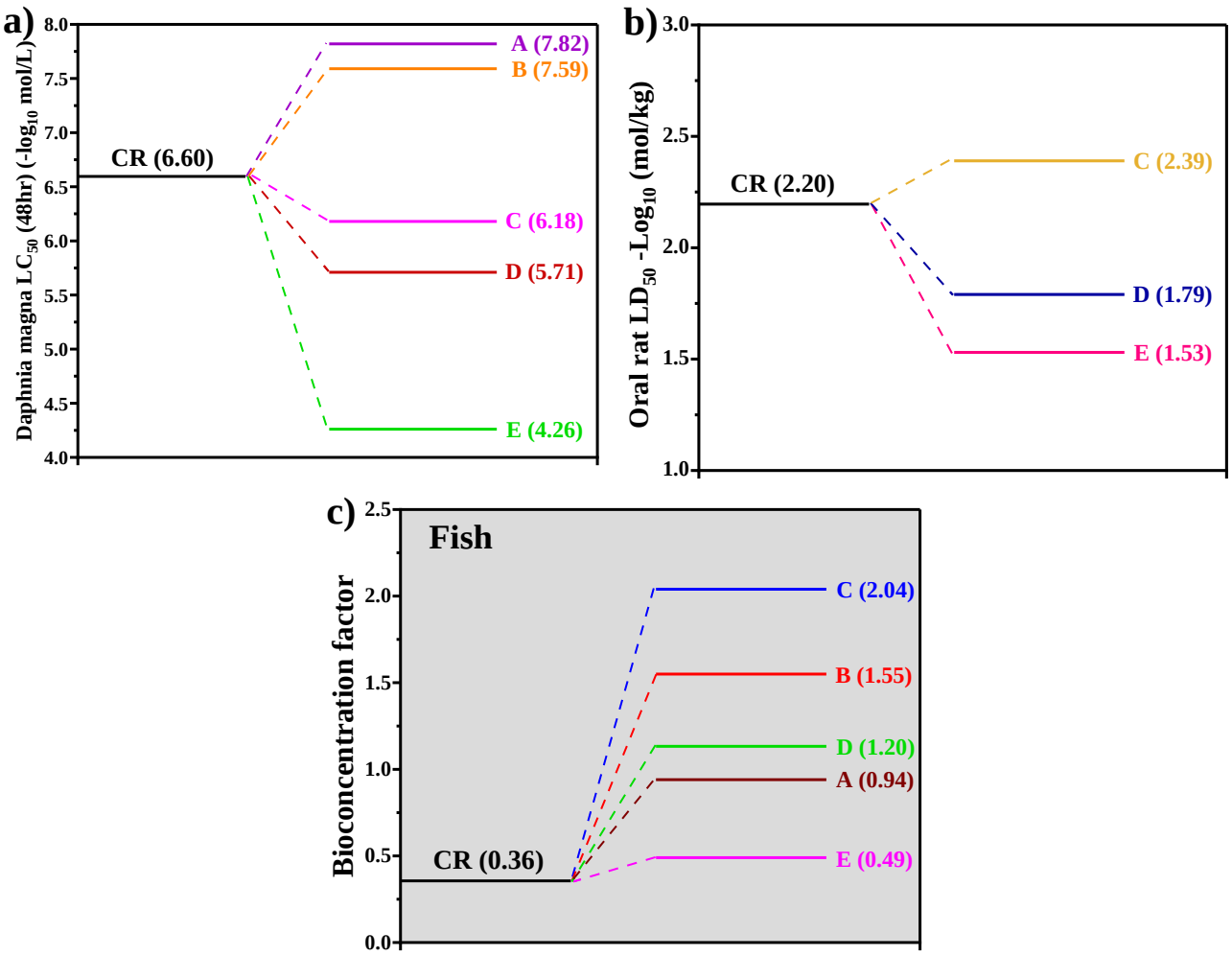

Fig. 14. Theoretical predicted a) Daphnia magna LC_{50} (48hr), b) Oral rat LD_{50} and c) Bioconcentration factor of Congo red and its intermediates.

Conclusion

This study demonstrated the efficient application of $ZnMn_2O_4$ as a photocatalyst for the solar-driven degradation of Congo Red (CR), achieving, 87.50% removal within 180 min. The degradation efficiency was significantly enhanced under acidic conditions, with complete dye elimination at pH 2. Scavenger experiments identified photogenerated holes (h^+) and hydroxyl radicals ($^{\bullet}OH$) as the primary reactive species driving the degradation process. $ZnMn_2O_4$

demonstrated good reusability, exhibiting only a 9% decline in activity over multiple cycles. Furthermore, DFT calculations confirmed the electron-accepting nature of Congo Red (CR), as evidenced by its higher LUMO energy (-2.6250 eV) compared to its HOMO energy (-3.1365 eV). Fukui function analysis identified nitrogen atoms as the most reactive sites, highlighting their role in electron transfer processes. Monte Carlo and Molecular Dynamics simulations provided further insight into dye-surface interactions, demonstrating stronger binding and greater affinity of Congo Red to the $ZnMn_2O_4$ surface relative to Rhodamine B, in agreement with experimental observations. Additionally, ecotoxicity assessment of Congo Red revealed that its degradation products exhibit significantly reduced toxicity relative to the parent dye.

CRediT authorship contribution statement

N. Ahmia: Investigation, Formal analysis, Writing - Original Draft. **M. Benamira:** Investigation, Formal analysis, Conceptualization, Supervision, Writing- Reviewing and Editing. **L. Messaadia, R. Masmoudi:** Investigation, Software. **D. Horwat:** Investigation, Validation. **I. Avramova** : Investigation; Validation.

Declaration of Competing Interest

The authors declare that they have no known competing financial interests or personal relationships that could have appeared to influence the work reported in this paper.

Acknowledgments

The authors thank the financial support of the Thematic Agency for Research in Science and Technology (ATRST) of Algeria through the project: PRFU N° B00L01UN180120220001.

Data availability

Data will be made available on request.

References

[1] R. Arunadevi, B. Kavitha, M. Rajarajan, A. Suganthi, and A. Jeyamurugan, “Investigation of the drastic improvement of photocatalytic degradation of Congo red by monoclinic Cd, Ba-CuO nanoparticles and its antimicrobial activities,” Surfaces and Interfaces, vol. 10, pp. 32–44, 2018, doi: 10.1016/j.surfin.2017.11.004.

[2] S. I. Siddiqui et al., “Investigation of Congo Red Toxicity towards Different Living Organisms: A Review,” Processes, vol. 11, no. 3, pp. 1–12, 2023, doi: 10.3390/pr11030807.

[3] N. Tara, S. I. Siddiqui, G. Rathi, S. A. Chaudhry, Inamuddin, and A. M. Asiri, “Nano-engineered adsorbent for the removal of dyes from water: A review,” Curr. Anal. Chem., vol. 16, no. 1, pp. 14–40, Feb. 2020, doi: 10.2174/1573411015666190117124344/CITE/REFWORKS.

[4] Y. Yang, K. Liu, F. Sun, Y. Liu, and J. Chen, “Enhanced performance of photocatalytic treatment of Congo red wastewater by CNTs-Ag-modified TiO2 under visible light,” Environ. Sci. Pollut. Res., vol. 29, no. 11, pp. 15516–15525, 2022, doi: 10.1007/s11356-021-16734-w.

[5] E. Palma Soto, C. A. Rodriguez Gonzalez, P. A. Luque Morales, H. Reyes Blas, and A. Carrillo Castillo, “Degradation of Organic Dye Congo Red by Heterogeneous Solar Photocatalysis with Bi2S3, Bi2S3/TiO2, and Bi2S3/ZnO Thin Films,” Catalysts, vol. 14, no. 9, p. 589, 2024, doi: 10.3390/catal14090589.

[6] G. E. Quintanilla-Villanueva, A. Sicardi-Segade, D. Luna-Moreno, R. E. Núñez-Salas, J. F. Villarreal-Chiu, and M. M. Rodríguez-Delgado, “Recent Advances in Congo Red Degradation by TiO2-Based Photocatalysts Under Visible Light,” Catalysts, vol. 15, no. 1, pp. 1–21, 2025, doi: 10.3390/catal15010084.

[7] N. Hokonya, C. Mahamadi, N. Mukaratirwa-Muchanyereyi, T. Gutu, and C. Zvinowanda, “Green synthesis of P − ZrO2CeO2ZnO nanoparticles using leaf extracts of Flacourtia indica and their application for the photocatalytic degradation of a model toxic dye, Congo red,” Heliyon, vol. 8, no. 8, 2022, doi: 10.1016/j.heliyon.2022.e10277.

[8] L. Messaadia et al., “Solar photodegradation of Rhodamine B dye by Cu2O/TiO2 heterostructure: experimental and computational studies of degradation and toxicity,” J. Mol. Model., vol. 29, no. 2, 2023, doi: 10.1007/s00894-023-05449-z.

[9] H. Lahmar et al., “Synthesis and characterization of CuAl2O4 nanoparticles : Application for the removal of Eriochrome Black T under solar light irradiation,” Inorg. Chem. Commun., vol. 163, p. 112316, 2024, doi: 10.1016/j.inoche.2024.112316.

[10] S. Kiamouche, L. Messaadia, H. Lahmar, G. Rekhila, M. Trari, and M. Benamira, “Enhanced photocatalytic degradation of Ponceau S Red dye on the novel hetero-system Fe2O3/WO3 under solar light irradiation,” React. Kinet. Mech. Catal., vol. 135, no. 6, pp. 3411–3426, 2022, doi: 10.1007/s11144-022-02313-8.

[11] H. Boulahbel et al., “Enhanced photodegradation of Congo red dye under sunlight irradiation by p-n NiFe2O4/TiO2 heterostructure,” Inorg. Chem. Commun., vol. 154, p. 110921, 2023, doi: 10.1016/j.inoche.2023.110921.

[12] H. Lahmar, S. Douafer, M. Benamira, A. Sahmi, and M. Trari, “Photo-Reduction of Cr (VI) on the novel hetero-System BaCr2O4/TiO2 under solar light irradiation,” Inorg. Chem. Commun., vol. 174, p. 113937, 2025, doi: 10.1016/j.inoche.2025.113937.

[13] H. Lahmar et al., “Photocatalytic degradation of crystal violet dye on the novel CuCr2O4/SnO2 hetero-system under sunlight,” Optik (Stuttg)., vol. 219, p. 165042, 2020, doi: 10.1016/j.ijleo.2020.165042.

[14] K. Rouibah et al., “Solar photocatalytic degradation of Methyl green on CuFe2O4/α Fe2O3 heterojunction,” Inorg. Chem. Commun., vol. 148, p. 110361, 2023, doi: 10.1016/j.inoche.2022.110361.

[15] F. Z. Akika, M. Benamira, H. Lahmar, M. Trari, I. Avramova, and Suzer, “Structural and optical properties of Cu-doped ZnAl2O4 and its application as photocatalyst for Cr (VI) reduction under sunlight,” Surfaces and Interfaces, vol. 18, p. 100406, 2020, doi: 10.1016/j.surfin.2019.100406.

[16] R. Gherbi, M. Benamira, and Y. Bessekhouad, “Enhanced photoelectrochemical and photocatalytic properties of Mg-doped ZnMn2O4,” J. Alloys Compd., vol. 851, p. 156797, 2021, doi: 10.1016/j.jallcom.2020.156797.

[17] R. Rashad, M. Khan, H. Qamar, and A. Hameed, “Biological and Photocatalytic Degradation of Congo Red , a Diazo Sulfonated Substituted Dye : a Review,” Water, Air, Soil Pollut., 2022, doi: 10.1007/s11270-022-05935-9.

[18] S. Boudiaf et al., “Kinetic studies of Congo Red Photodegradation on the hetero-system CoAl2O4/ZnO with a stirred reactor under solar light,” J. Environ. Chem. Eng., vol. 9, no. 4, p. 105572, 2021, doi: 10.1016/j.jece.2021.105572.

[19] E. S. Al-Farraj and E. A. Abdelrahman, “Efficient Photocatalytic Degradation of Congo Red Dye Using Facilely Synthesized and Characterized MgAl2O4 Nanoparticles,” ACS Omega, vol. 9, no. 4, pp. 4870–4880, 2024, doi: 10.1021/acsomega.3c08485.

[20] A. Zia, A. B. Naveed, A. Javaid, M. F. Ehsan, and A. Mahmood, “Facile Synthesis of ZnSe/Co3O4 Heterostructure Nanocomposites for the Photocatalytic Degradation of Congo Red Dye,” Catalysts, vol. 12, no. 10, p. 1184, 2022, doi: 10.3390/catal12101184.

[21] R. S. Brishti et al., “Green synthesis of ZnO NPs using aqueous extract of Epipremnum aureum leave: Photocatalytic degradation of Congo red,” Results Chem., vol. 7, p. 101441, 2024, doi: 10.1016/j.rechem.2024.101441.

[22] M. Akhter, M. K. Amin, P. K. Dhar, S. K. Dey, M. S. Hossain, and S. K. Dutta, “Fabrication of rare-earth cerium-doped nickel-copper ferrite as a promising photo-catalyst for congo red-containing wastewater treatment,” RSC Adv., vol. 14, no. 40, pp. 29083–29098, 2024, doi: 10.1039/d4ra04334k.

[23] S. Hemamalini and R. Manimekalai, “Synthesis, physicochemical and photocatalytic activities of nano ZnCo2O4 catalyst for photodegradation of various dyes under sunlight irradiation,” Bull. Mater. Sci., vol. 44, no. 2, p. 154, 2021, doi: 10.1007/s12034-021-02453-y.

[24] N. Ahmia et al., “Photocatalytic activity of ZnMn2O4/TiO2 heterostructure under solar light irradiation: Experimental and theoretical study,” J. Mol. Struct., vol. 1306, p.

137834, 2024, doi: 10.1016/j.molstruc.2024.137834.

[25] A. Sobhani and S. Alinavaz, “ZnMn2O4 nanostructures: Synthesis via two different chemical methods, characterization, and photocatalytic applications for the degradation of new dyes,” Heliyon, vol. 9, no. 11, 2023, doi: 10.1016/j.heliyon.2023.e21979.

[26] N. Senthilkumar, V. Venkatachalam, M. Kandiban, P. Vigneshwaran, R. Jayavel, and I. Vetha Potheher, “Studies on electrochemical properties of hetarolite (ZnMn2O4) nanostructure for supercapacitor application,” Phys. E Low-Dimensional Syst. Nanostructures, vol. 106, pp. 121–126, 2019, doi: 10.1016/j.physe.2018.10.027.

[27] C. Liang, J. Chen, K. Yu, and W. Jin, “ZnMn2O4 spheres anchored on jute porous carbon for use as a high-performance anode material in lithium-ion batteries,” J. Alloys Compd., vol. 878, p. 160445, 2021, doi: 10.1016/j.jallcom.2021.160445.

[28] R. Gherbi, Y. Bessekhouad, and M. Trari, “Structure, optical and transport properties of Mg-doped ZnMn2O4,” J. Alloys Compd., vol. 655, pp. 188–197, 2016, doi: 10.1016/j.jallcom.2015.09.192.

[29] F. Zhu, J. Ma, Q. Ji, H. Cheng, and S. Komarneni, “Visible-light-driven activation of sodium persulfate for accelerating orange II degradation using ZnMn2O4 photocatalyst,” Chemosphere, vol. 278, p. 130404, 2021, doi: 10.1016/j.chemosphere.2021.130404.

[30] A. Haleem et al., “In-Depth Photocatalytic Degradation Mechanism of the Extensively Used Dyes Malachite Green, Methylene Blue, Congo Red, and Rhodamine B via Covalent Organic Framework-Based Photocatalysts,” Water, vol. 16, no. 11, p. 1588, 2024.

[31] M. Y. Nassar, E. A. El-Moety, and M. F. El-Shahat, “Synthesis and characterization of a ZnMn2O4 nanostructure as a chemical nanosensor: A facile and new approach for colorimetric determination of omeprazole and lansoprazole drugs,” RSC Adv., vol. 7, no. 69, pp. 43798–43811, 2017, doi: 10.1039/c7ra08010g.

[32] S. Nazir, J.-M. Zhang, K. Qadir, S. Saleem, Investigation of structural, morphological and optical properties of Ni-doped ZnFe2O4 nanoparticles synthesized by sol-gel auto-combustion method, Phys. Met. Metallogr. 125 (2024) S13–S20.

[33] S. S. Hussein and E. K. Al-Shakarchi, “Sol gel auto combustion method to prepare nanostructures LiZnCu ferrite,” Ceram. Int., vol. 50, no. 10, pp. 17913–17923, 2024, doi: 10.1016/J.CERAMINT.2024.02.280.

[34] A. R. Chavan, S. B. Bhosale, S. B. Somvanshi, and P. P. Khirade, “Effect of Zr4+ dopants on micro-structural and antibacterial characteristics of CuFe2O4 nanoparticles produced via sol-gel auto combustion,” J. Sol-Gel Sci. Technol., pp. 1–14, 2025, doi: 10.1007/S10971-025-06730-8/METRICS.

[35] P. Nunocha, M. Kaewpanha, T. Bongkarn, A. Phuruangrat, T. Suriwong, A new route to synthesizing La-doped SrTiO3 nanoparticles using the sol-gel auto combustion method and their characterization and photocatalytic application, Mater. Sci. Semicond. Process.

134 (2021) 106001. https://doi.org/10.1016/j.mssp.2021.106001.

[36] I. Salahshoori, Q. Wang, M. A. L. Nobre, A. H. Mohammadi, E. A. Dawi, and H. A. Khonakdar, "Molecular simulation-based insights into dye pollutant adsorption: A perspective review," Adv. Colloid Interface Sci., p. 103281, 2024, doi: 10.1016/j.cis.2024.103281.

[37] K. Zhang, "Learning thermodynamics and topological order of the two-dimensional XY model with generative real-valued restricted Boltzmann machines," Phys. Rev. B, vol. 111, no. 2, p. 024112, 2025, doi: 10.1103/PHYSREVB.111.024112/FIGURES/11/THUMBNAIL.

[38] A. Chahid, M. Chafi, M. Essahli, A. A. Alrashdi, and H. Lgaz, "Exploring the efficacy of Congo Red dye as a corrosion inhibitor for aluminum in HCl solution: An interdisciplinary study with RSM modeling and theoretical simulations," Arab. J. Chem., vol. 17, no. 7, p. 105810, 2024, doi: 10.1016/j.arabjc.2024.105810.

[39] D. Sibanda, S. T. Oyinbo, and T. C. Jen, "A review of atomic layer deposition modelling and simulation methodologies: Density functional theory and molecular dynamics," Nanotechnol. Rev., vol. 11, no. 1, pp. 1332–1363, 2022, doi: 10.1515/ntrev-2022-0084.

[40] Y. Liu, W. Hong, and B. Cao, "Machine learning for predicting thermodynamic properties of pure fluids and their mixtures," Energy, vol. 188, p. 116091, 2019, doi: 10.1016/j.energy.2019.116091.

[41] M. von Domaros, D.J. Tobias, Molecular Dynamics Simulations of the Interactions of Organic Compounds at Indoor Relevant Surfaces, Annu. Rev. Phys. Chem. 76 (2025) 231–250. https://doi.org/10.1146/annurev-physchem-083122-123017.

[42] R. Hsissou, F. Benhiba, M. El Aboubi, S. Abbout, Z. Benzekri, Z. Safi, M. Rafik, H. Bahaj, M. Kaba, M. Galai, N. Wazzan, S. Briche, S. Boukhris, A. Zarrouk, M. EbnTouhami, M. Rafik, Synthesis and performance of two ecofriendly epoxy resins as a highly efficient corrosion inhibition for carbon steel in 1 M HCl solution: DFT, RDF, FFV and MD approaches, Chem. Phys. Lett. 806 (2022) 139995. https://doi.org/10.1016/j.cplett.2022.139995.

[43] J. I. Martínez-Araya, "Why is the dual descriptor a more accurate local reactivity descriptor than Fukui functions?," J. Math. Chem., vol. 53, no. 2, pp. 451–465, 2015, doi: 10.1007/S10910-014-0437-7/METRICS.

[44] G. Harini et al., "Enhanced photodegradation of rifampicin and co-trimoxazole by ZnO/ZnMn2O4/ZnS-PVA and its genotoxicity studies on Allium cepa," Chemosphere, vol. 308, p. 136238, 2022, doi: 10.1016/j.chemosphere.2022.136238.

[45] R. Manna, G. Bhattacharya, P. Sardar, S. Rahut, and A. N. Samanta, "Photocatalytic performance and mechanism insights of an S-scheme ZnMn2O4/ZIF-67 heterostructure in photocatalytic CO2 reduction under visible light irradiation," Renew. Energy, vol. 229, p. 120752, 2024, doi: 10.1016/j.renene.2024.120752.

[46] S. Raj, R. Manna, and A. N. Samanta, “Spinel ZnMn2O4 nanosphere for the efficient Sulfamethazine degradation under visible light irradiation and photoelectrochemical study,” J. Environ. Chem. Eng., vol. 12, no. 2, p. 112277, 2024, doi: 10.1016/j.jece.2024.112277.

[47] M. Benamira et al., “Hydrogen production on the new hetero-system Pr2NiO4/SnO2 under visible light irradiation,” Int. J. Hydrogen Energy, vol. 45, no. 3, pp. 1719–1728, 2020, doi: 10.1016/j.ijhydene.2019.11.064.

[48] H. Lahmar, M. Benamira, L. Messaadia, M. Hamdi, I. Avramova, and M. Trari, “Synthesis, physical and photo-electrochemical properties of Gd2CuO4,” J. Alloys Compd., vol. 816, p. 152629, 2020, doi: 10.1016/j.jallcom.2019.152629.

[49] S. Alkaykh, A. Mbarek, and E. E. Ali-Shattle, “Photocatalytic degradation of methylene blue dye in aqueous solution by MnTiO3 nanoparticles under sunlight irradiation,” Heliyon, vol. 6, no. 4, 2020, doi: 10.1016/j.heliyon.2020.e03663.

[50] A. Sinha, S. K. Sahu, S. Biswas, and T. K. Ghorai, “Synthesis of CeO2/ZrO2/ZnO nano alloy oxide and investigation of photocatalysis of naphthol orange under sunlight,” RSC Adv., vol. 13, no. 32, pp. 22029–22042, 2023, doi: 10.1039/d3ra03579d.

[51] S. Habi Ben Hariz, H. Lahmar, G. Rekhila, A. Bouhala, M. Trari., and M. Benamira, “A novel MgCr2O4/WO3 hetero-junction photocatalyst for solar photo reduction of hexavalent chromium Cr(VI),” J. Photochem. Photobiol. A Chem., vol. 430, p. 113986, 2022, doi: 10.1016/j.jphotochem.2022.113986.

[52] M. Saeed, M. Muneer, A. ul Haq, and N. Akram, “Photocatalysis : an effective tool for photodegradation of dyes — a review,” Environ. Sci. Pollut. Res., vol. 29, no. 1, pp. 293–311, 2022.

[53] A.J. Bard, R. Parsons, J. Jordan, Standard Potentials in Aqueous Solution, Routledge, 2017. https://doi.org/10.1201/9780203738764.

[54] N. Ali et al., “Photocatalytic Degradation of Congo Red Dye from Aqueous Environment Using Cobalt Ferrite Nanostructures: Development, Characterization, and Photocatalytic Performance,” Water. Air. Soil Pollut., vol. 231, no. 2, 2020, doi: 10.1007/s11270-020-4410-8.

[55] J. Khan, K. Tahir, Y. Wei, K. Albalawi, S. Latif, F. Abdulaziz, A.A. El-Zahhar, E. Abdu Musad Saleh, H.S. Al-Shehri, M.M. Alghamdi, Preparation of Ca0.1Cu0.90Bi2O4 heterojunction with improved visible light photocatalytic performance of congo red: Kinetics and degradation mechanisms, Inorg. Chem. Commun. 142 (2022) 109607. https://doi.org/10.1016/j.inoche.2022.109607.

[56] H. Li, Y. Zhao, C. Yin, L. Jiao, and L. Ding, “WO3 nanocrystal prepared by self-assembly of phosphotungstic acid and dopamine for photocatalytic degradation of Congo red,” Colloids Surfaces A Physicochem. Eng. Asp., vol. 572, pp. 147–151, 2019, doi: 10.1016/j.colsurfa.2019.03.092.

[57] R. Benisha, M. Amalanathan, M. Aravind, M.S.M. Mary, A. Ahmad, S. Tabassum, W.H. Al-Qahtani, I. Ahmad, Catharanthus roseus leaf extract mediated Ag-MgO nanocatalyst for photocatalytic degradation of Congo red dye and their antibacterial activity, J. Mol. Struct. 1262 (2022) 133005. https://doi.org/10.1016/j.molstruc.2022.133005.

[58] S. Kiamouche et al., "Cu2O@Zn-Fe LDH Core-Shell photocatalyst for solar photo-degradation of Congo Red: An experimental, DFT, and Monte Carlo combined simulation," J. Mol. Struct., vol. 1342, p. 142701, 2025, doi: 10.1016/j.molstruc.2025.142701.

[59] H. Tandon, T. Chakraborty, and V. Suhag, "A fundamental approach to compute atomic electrophilicity index," J. Math. Chem., vol. 58, pp. 2188–2196, 2020, doi: 10.1007/S10910-020-01176-5/METRICS.

[60] F. Rehman, M. Sayed, J. A. Khan, N. S. Shah, H. M. Khan, and D. D. Dionysiou, "Oxidative removal of brilliant green by UV/S2O82–, UV/HSO5– and UV/H2O2 processes in aqueous media: A comparative study," J. Hazard. Mater., vol. 357, pp. 506–514, 2018, doi: 10.1016/j.jhazmat.2018.06.012.

[61] Z. U. H. Khan et al., "Photocatalytic and biomedical investigation of green synthesized NiONPs: Toxicities and degradation pathways of Congo red dye," Surfaces and Interfaces, vol. 23, p. 100944, 2021, doi: 10.1016/j.surfin.2021.100944.

[62] N. S. Shah et al., "Synergistic effects of H2O2 and S2O82− in the gamma radiation induced degradation of congo-red dye : Kinetics and toxicities evaluation," Sep. Purif. Technol., vol. 233, p. 115966, 2020, doi: 10.1016/j.seppur.2019.115966.

[63] J. Li, J. Liu, T. Pan, X. Zhang, H. Zheng, and L. Feng, "Electrocatalytically enhanced Cu(II)/peroxymonosulfate (PMS) oxidation: Focus on electrically-induced sustained Cu(II)/Cu(I)/Cu(III) cycling and suppression of singlet oxygen (1O2) production," Sep. Purif. Technol., vol. 342, p. 127093, 2024, doi: 10.1016/j.seppur.2024.127093.